

# AGATA – Advanced Gamma Tracking Array

S. Akkoyun<sup>a</sup>, A. Algora<sup>b</sup>, B. Alikhani<sup>c</sup>, F. Ameil<sup>d</sup>, G. de Angelis<sup>e</sup>, L. Arnold<sup>f,g</sup>, A. Astier<sup>h</sup>, A. Ata<sup>a,i,j</sup>, Y. Aubert<sup>k</sup>, C. Aufranc<sup>m</sup>, A. Austin<sup>n</sup>, S. Aydin<sup>o</sup>, F. Azaiez<sup>k</sup>, S. Badoer<sup>e</sup>, D.L. Balabanski<sup>p</sup>, D. Barrientos<sup>b</sup>, G. Baulieu<sup>m</sup>, R. Baumann<sup>f,g</sup>, D. Bazzacco<sup>o</sup>, F.A. Beck<sup>f,g</sup>, T. Beck<sup>d</sup>, P. Bednarczyk<sup>q</sup>, M. Bellato<sup>o</sup>, M.A. Bentley<sup>r</sup>, G. Benzoni<sup>s</sup>, R. Berthier<sup>t</sup>, L. Berti<sup>e</sup>, R. Beunard<sup>u</sup>, G. Lo Bianco<sup>v,1</sup>, B. Birkenbach<sup>w</sup>, P.G. Bizzeti<sup>x,y</sup>, A.M. Bizzeti-Sona<sup>x,y</sup>, F. Le Blanc<sup>k</sup>, J.M. Blasco<sup>z</sup>, N. Blasi<sup>s</sup>, D. Bloor<sup>c</sup>, C. Boiano<sup>s</sup>, M. Borsato<sup>aa</sup>, D. Bortolato<sup>o,aa</sup>, A.J. Boston<sup>ab,\*</sup>, H.C. Boston<sup>ab</sup>, P. Bourgauff<sup>u</sup>, P. Boutachkov<sup>d,c</sup>, A. Bouty<sup>t</sup>, A. Bracco<sup>s,ac</sup>, S. Brambilla<sup>s</sup>, I.P. Brawn<sup>ad</sup>, A. Brondi<sup>ae</sup>, S. Broussard<sup>t</sup>, B. Bruyneel<sup>w</sup>, D. Bucurescu<sup>af</sup>, I. Burrows<sup>n</sup>, A. Bürger<sup>t,ag,ah</sup>, S. Cabaret<sup>h</sup>, B. Cahan<sup>u</sup>, E. Calore<sup>e</sup>, F. Camera<sup>s,ac</sup>, A. Capsoni<sup>s</sup>, F. Carrió<sup>z</sup>, G. Casati<sup>s,ai</sup>, M. Castoldi<sup>aj</sup>, B. Cederwall<sup>l</sup>, J.-L. Cercus<sup>k</sup>, V. Chambert<sup>k</sup>, M. El Chambit<sup>f,g</sup>, R. Chapman<sup>ak</sup>, L. Charles<sup>f,g</sup>, J. Chavas<sup>o</sup>, E. Clément<sup>u</sup>, P. Cocconi<sup>e</sup>, S. Coelli<sup>s</sup>, P.J. Coleman-Smith<sup>n</sup>, A. Colombo<sup>o</sup>, S. Colosimo<sup>ab</sup>, C. Commeaux<sup>b</sup>, D. Conventi<sup>o</sup>, R.J. Cooper<sup>ab</sup>, A. Corsi<sup>s,ac</sup>, A. Cortesi<sup>s</sup>, L. Costa<sup>e</sup>, F.C.L. Crespi<sup>s,ac</sup>, J.R. Cresswell<sup>ab</sup>, D.M. Cullen<sup>al</sup>, D. Curien<sup>f,g</sup>, A. Czermak<sup>q</sup>, D. Delbourg<sup>k</sup>, R. Depalo<sup>am</sup>, T. Descombes<sup>an</sup>, P. Désesquelles<sup>h</sup>, P. Detistov<sup>p</sup>, C. Diarra<sup>k</sup>, F. Didierjean<sup>f,g</sup>, M.R. Dimmock<sup>ab</sup>, Q.T. Doan<sup>m</sup>, C. Domingo-Pardo<sup>b,d</sup>, M. Doncel<sup>ao</sup>, F. Dorangeville<sup>k</sup>, N. Dosme<sup>h</sup>, Y. Drouen<sup>t</sup>, G. Duchêne<sup>f,g,\*</sup>, B. Dulny<sup>q</sup>, J. Eberth<sup>w</sup>, P. Edelbruck<sup>k</sup>, J. Egea<sup>b,z</sup>, T. Engert<sup>d</sup>, M.N. Erduran<sup>ap</sup>, S. Ertürk<sup>aq</sup>, C. Fanin<sup>o</sup>, S. Fantinel<sup>e</sup>, E. Farnea<sup>o,s</sup>, T. Faul<sup>f,g</sup>, M. Filliger<sup>f,g</sup>, F. Filmer<sup>ab</sup>, Ch. Finck<sup>f,g</sup>, G. de France<sup>u</sup>, A. Gadea<sup>e,b,\*</sup>, W. Gast<sup>tr</sup>, A. Geraci<sup>s,ai</sup>, J. Gerl<sup>d</sup>, R. Gernhäuser<sup>as</sup>, A. Giannatiempo<sup>x,y</sup>, A. Giaz<sup>s,ac</sup>, L. Gibelin<sup>h</sup>, A. Givechev<sup>c</sup>, N. Goel<sup>d,c</sup>, V. González<sup>z</sup>, A. Gottardo<sup>c</sup>, X. Grave<sup>k</sup>, J. Grębosz<sup>d</sup>, R. Griffiths<sup>n</sup>, A.N. Grint<sup>ab</sup>, P. Gros<sup>t</sup>, L. Guevara<sup>k</sup>, M. Gulmini<sup>e</sup>, A. Görgen<sup>t</sup>, H.T.M. Ha<sup>h</sup>, T. Habermann<sup>d</sup>, L.J. Harkness<sup>ab</sup>, H. Harroch<sup>k</sup>, K. Hauschild<sup>h</sup>, C. He<sup>e</sup>, A. Hernández-Prieto<sup>ao</sup>, B. Hervieu<sup>t</sup>, H. Hess<sup>w</sup>, T. Hüyük<sup>b</sup>, E. Ince<sup>ap,c</sup>, R. Isocrate<sup>o</sup>, G. Jaworski<sup>at,au</sup>, A. Johnson<sup>j</sup>, J. Jolie<sup>w</sup>, P. Jones<sup>av</sup>, B. Jonson<sup>aw</sup>, P. Joshi<sup>r</sup>, D.S. Judson<sup>ab</sup>, A. Jungclaus<sup>ax</sup>, M. Kaci<sup>b</sup>, N. Karkour<sup>h</sup>, M. Karolak<sup>t</sup>, A. Kaşkaş<sup>a</sup>, M. Kebbiri<sup>t</sup>, R.S. Kempley<sup>ay</sup>, A. Khaplanov<sup>l</sup>, S. Klupp<sup>as</sup>, M. Kogimtzis<sup>n</sup>, I. Kojouharov<sup>d</sup>, A. Korichi<sup>h,\*</sup>, W. Korten<sup>t</sup>, Th. Kröll<sup>o,e</sup>, R. Krücker<sup>as</sup>, N. Kurz<sup>d</sup>, B.Y. Ky<sup>k</sup>, M. Labiche<sup>n</sup>, X. Lafay<sup>h</sup>, L. Lavergne<sup>k</sup>, I.H. Lazarus<sup>n</sup>, S. Leboutelier<sup>h</sup>, F. Lefebvre<sup>k</sup>, E. Legay<sup>h</sup>, L. Legeard<sup>u</sup>, F. Lelli<sup>e</sup>, S.M. Lenzi<sup>o,aa</sup>, S. Leoni<sup>s,ac</sup>, A. Lermite<sup>g</sup>, D. Lersch<sup>w</sup>, J. Leske<sup>c</sup>, S.C. Letts<sup>n</sup>, S. Lhenoret<sup>h</sup>, R.M. Liedner<sup>af</sup>, D. Linget<sup>h</sup>, J. Ljungvall<sup>ht</sup>, A. Lopez-Martens<sup>h</sup>, A. Lotodé<sup>t</sup>, S. Lunardi<sup>o,aa</sup>, A. Maj<sup>q</sup>, J. van der Mare<sup>l</sup>, Y. Mariette<sup>t</sup>, N. Marginean<sup>af</sup>, R. Marginean<sup>o,aa,af</sup>, G. Maron<sup>e</sup>, A.R. Mather<sup>ab</sup>, W. Męczyński<sup>d</sup>, V. Mendéz<sup>b</sup>, P. Medina<sup>f,g</sup>, B. Melon<sup>x,y</sup>, R. Menegazzo<sup>o</sup>, D. Mengoni<sup>o,aa,ak</sup>, E. Merchan<sup>d,c</sup>, L. Mihailescu<sup>ar,2</sup>, C. Michelagnoli<sup>o,aa</sup>, J. Mierzejewski<sup>au</sup>, L. Milechina<sup>l</sup>, B. Million<sup>s</sup>, K. Mitev<sup>az</sup>, P. Molini<sup>c</sup>, D. Montanari<sup>s,ac</sup>, S. Moon<sup>ab</sup>, F. Morbiducci<sup>h</sup>, R. Moro<sup>ae</sup>, P.S. Morrar<sup>n</sup>, O. Möller<sup>c</sup>, A. Nannini<sup>y</sup>, D. R. Napoli<sup>e</sup>, L. Nelson<sup>ab</sup>, M. Nespolo<sup>o,aa</sup>, V.L. Ngo<sup>h</sup>, M. Nicoletto<sup>o</sup>, R. Nicolini<sup>s,ac</sup>, Y. Le Noa<sup>t</sup>, P.J. Nolan<sup>ab</sup>, M. Norman<sup>ab</sup>, J. Nyberg<sup>i,\*\*</sup>, A. Obertelli<sup>t</sup>, A. Olariu<sup>k</sup>, R. Orlandi<sup>ak,ax</sup>, D.C. Oxley<sup>ab</sup>, C. Özben<sup>ba</sup>, M. Ozille<sup>u</sup>, C. Oziol<sup>k</sup>, E. Pachoud<sup>f,g</sup>, M. Palacz<sup>au</sup>, J. Palin<sup>n</sup>, J. Pancer<sup>u</sup>, C. Parisel<sup>f,g</sup>, P. Parisel<sup>h</sup>, G. Pascovici<sup>w</sup>, R. Peghin<sup>o</sup>, L. Pellegrini<sup>s,ac</sup>, A. Perego<sup>x,y</sup>, S. Perrier<sup>h</sup>, M. Petcu<sup>af</sup>, P. Petkov<sup>p</sup>, C. Pettrache<sup>k</sup>, E. Pierre<sup>h</sup>, N. Pietralla<sup>c</sup>, S. Pietri<sup>d</sup>, M. Pignatelli<sup>s,ac</sup>, I. Piqueras<sup>f,g</sup>, Z. Podolyak<sup>ay</sup>, P. Le Pouhalec<sup>t</sup>, J. Pouthas<sup>sk</sup>, D. Pugnère<sup>m</sup>, V.F.E. Pucknell<sup>n</sup>, A. Pullia<sup>s,ac</sup>, B. Quintana<sup>ao</sup>, R. Raine<sup>u</sup>, G. Rainovski<sup>az</sup>, L. Ramina<sup>o</sup>, G. Rampazzo<sup>o</sup>, G.La Rana<sup>ae</sup>, M. Rebeschini<sup>o</sup>, F. Recchia<sup>o,aa</sup>, N. Redon<sup>m</sup>, M. Reese<sup>c</sup>, P. Reiter<sup>w,\*</sup>, P.H. Regan<sup>ay</sup>, S. Riboldi<sup>s,ac</sup>, M. Richer<sup>f,g</sup>, M. Rigato<sup>e</sup>, S. Rigby<sup>ab</sup>, G. Ripamonti<sup>s,ai</sup>, A.P. Robinson<sup>al</sup>, J. Robin<sup>f,g</sup>, J. Roccaz<sup>h</sup>, J.-A. Ropert<sup>u</sup>, B. Rossé<sup>m</sup>, C. Rossi Alvarez<sup>o</sup>, D. Rosso<sup>e</sup>, B. Rubio<sup>p</sup>, D. Rudolph<sup>bb</sup>, F. Saillant<sup>u</sup>, E. Şahin<sup>e</sup>, F. Salomon<sup>k</sup>, M.-D. Salsac<sup>t</sup>, J. Salt<sup>b</sup>, G. Salvato<sup>o,aa</sup>, J. Sampson<sup>ab</sup>, E. Sanchis<sup>z</sup>, C. Santos<sup>f,g</sup>, H. Schaffner<sup>d</sup>, M. Schlarb<sup>as</sup>, D.P. Scraggs<sup>ab</sup>, D. Seddon<sup>ab</sup>, M. Şenyigit<sup>a</sup>, M.-H. Sigward<sup>f,g</sup>, G. Simpson<sup>an</sup>, J. Simpson<sup>n,\*</sup>, M. Slee<sup>ab</sup>, J.F. Smith<sup>ak</sup>, P. Sona<sup>x,y</sup>, B. Sowicki<sup>q</sup>, P. Spolaore<sup>e</sup>, C. Stahl<sup>c</sup>, T. Stanios<sup>ab</sup>, E. Stefanova<sup>p</sup>, O. Stężowski<sup>m</sup>, J. Strachan<sup>n</sup>, G. Suliman<sup>af</sup>, P.-A. Söderström<sup>i</sup>, J.L. Tain<sup>b</sup>, S. Tanguy<sup>k</sup>, S. Tashenov<sup>jd</sup>, Ch. Theisen<sup>t</sup>, J. Thornhill<sup>ab</sup>, F. Tomasi<sup>s</sup>, N. Toniolo<sup>o</sup>, R. Touzery<sup>t</sup>, B. Travers<sup>h</sup>, A. Triossi<sup>o,aa</sup>, M. Tripone<sup>u</sup>, K.M.M. Tun-Lanoë<sup>kk</sup>, M. Turcato<sup>o</sup>, C. Unsworth<sup>ab</sup>, C.A. Ur<sup>o,af</sup>, J. J.Valiente-Dobon<sup>e</sup>, V. Vandone<sup>s,ac</sup>, E. Vardaci<sup>ae</sup>, R. Venturelli<sup>o,aa</sup>, F. Veronese<sup>o</sup>, Ch. Veysiere<sup>t</sup>, E. Viscione<sup>s</sup>, R. Wadsworth<sup>r</sup>, P.M. Walker<sup>ay</sup>, N. Warr<sup>w</sup>, C. Weber<sup>f,g</sup>, D. Weisshaar<sup>w,3</sup>, D. Wells<sup>ab</sup>, O. Wieland<sup>s</sup>, A. Wiens<sup>w</sup>, G. Wittner<sup>u</sup>, H.J. Wollersheim<sup>d</sup>, F. Zocca<sup>a</sup>, N.V. Zamfir<sup>af</sup>, M. Ziębliński<sup>d</sup>, A. Zucchiatti<sup>aj</sup>

<sup>a</sup>Department of Physics, Faculty of Science, Ankara University, 06100 Tandoğan, Ankara, Turkey

<sup>b</sup>IFIC, CSIC-Universitat de València, E-46980 Paterna, Spain

<sup>c</sup>IKP, TU Darmstadt, Schlossgartenstraße 9, D-64289 Darmstadt, Germany

<sup>d</sup>GSI Helmholtzzentrum für Schwerionenforschung GmbH, D-64291 Darmstadt, Germany

<sup>e</sup>INFN Laboratori Nazionali di Legnaro, IT-35020 Padova, Italy

<sup>f</sup>Université de Strasbourg, IPHC, 23 rue du Loess, 67037 Strasbourg, France

<sup>g</sup>CNRS, UMR 7178, 67037 Strasbourg, France

<sup>h</sup>CSNSM, CNRS, IN2P3, Université Paris-Sud, F-91405 Orsay, France

<sup>i</sup>Department of Physics and Astronomy, Uppsala University, Uppsala, Sweden

<sup>j</sup>The Royal Institute of Technology, SE-10691 Stockholm, Sweden

<sup>k</sup>IPNO, CNRS/IN2P3, Université Paris-Sud, F-91406 Orsay, France

<sup>m</sup>Université de Lyon, Université Lyon 1, CNRS-IN2P3, Institut de Physique Nucléaire de Lyon, F-69622 Villeurbanne, France

<sup>n</sup>STFC Daresbury Laboratory, Daresbury, Warrington WA4 4AD, UK

\*Corresponding authors

\*\*Principal corresponding author

Email addresses: a.j.boston@liverpool.ac.uk (A.J. Boston), gilbert.duchene@ires.in2p3.fr (G. Duchêne), enrico.farnea@padova.infn.it (E. Farnea), andres.gadea@ific.uv.es (A. Gadea), korichi@csnsm.in2p3.fr (A. Korichi), johan.nyberg@physics.uu.se (J. Nyberg), preiter@ikp.uni-koeln.de (P. Reiter), john.simpson@stfc.ac.uk (J. Simpson)

<sup>1</sup>Deceased

<sup>2</sup>Present address: Lawrence Berkeley National Laboratory, Berkeley, CA, USA

<sup>3</sup>Present address: National Superconducting Cyclotron Laboratory Michigan State University, East Lansing, Michigan 48824-1321, USA

- <sup>o</sup>INFN Sezione di Padova, IT-35131 Padova, Italy
- <sup>p</sup>Institute for Nuclear Research and Nuclear Energy, Bulgarian Academy of Sciences, Sofia, Bulgaria
- <sup>q</sup>The Henryk Niewodniczanski Institute of Nuclear Physics, Polish Academy of Sciences, ul. Radzikowskiego 152, 31-342 Kraków, Poland
- <sup>r</sup>Department of Physics, University of York, York, YO10 5DD, UK
- <sup>s</sup>INFN Sezione di Milano, IT-20133 Milano, Italy
- <sup>t</sup>CEA, Centre de Saclay, IRFU, F-91191 Gif-sur-Yvette, France
- <sup>u</sup>Grand Accélérateur National d'Ions Lourds (GANIL), CEA/DSM-CNRS/IN2P3, Bvd Henri Becquerel, 14076 Caen, France
- <sup>v</sup>Università di Camerino and INFN Sezione di Perugia, IT-06123 Perugia, Italy
- <sup>w</sup>IKP, University of Cologne, D-50937 Cologne, Germany
- <sup>x</sup>Università di Firenze, Dipartimento di Fisica e Astronomia, IT-50019 Firenze, Italy
- <sup>y</sup>INFN Sezione di Firenze, IT-50019 Firenze, Italy
- <sup>z</sup>Department of Electronic Engineering, University of Valencia, Burjassot (Valencia) Spain
- <sup>aa</sup>Dipartimento di Fisica, Università di Padova, IT-35131 Padova, Italy
- <sup>ab</sup>Oliver Lodge Laboratory, The University of Liverpool, Oxford Street, Liverpool L69 7ZE, UK
- <sup>ac</sup>Dipartimento di Fisica, Università di Milano, IT-20133 Milano, Italy
- <sup>ad</sup>STFC Rutherford Appleton Laboratory, Harwell, Didcot OX11 0QX, UK
- <sup>ae</sup>Dipartimento di Fisica dell'Università and INFN Sezione di Napoli, IT-80126 Napoli, Italy
- <sup>af</sup>National Institute of Physics and Nuclear Engineering, Bucharest-Magurele, Romania
- <sup>ag</sup>Helmholtz-Institut für Strahlen- und Kernphysik, Universität Bonn, Nußallee 14-16, D-53115 Bonn, Germany
- <sup>ah</sup>University of Oslo, Department of Physics, N-0316 Oslo, Norway
- <sup>ai</sup>Politecnico di Milano, Dipartimento di Elettronica e Informazione, IT-20133 Milano, Italy
- <sup>aj</sup>INFN Sezione di Genova, IT-16146 Genova, Italy
- <sup>ak</sup>School of Engineering, University of the West of Scotland, Paisley, PA1 2BE, UK
- <sup>al</sup>Schuster Laboratory, School of Physics and Astronomy, The University of Manchester, Manchester, M13 9PL, UK
- <sup>am</sup>Dipartimento di Astronomia, Università di Padova, IT-35131 Padova, Italy
- <sup>an</sup>LPSC, Université Joseph Fourier Grenoble 1, CNRS/IN2P3, INP Grenoble, F-38026 Grenoble Cedex, France
- <sup>ao</sup>Departamento de Física Fundamental, Universidad de Salamanca, Salamanca, Spain
- <sup>ap</sup>Istanbul University, Istanbul, Turkey
- <sup>aq</sup>Department of Physics, Science Faculty, Niğde University, 51200 Niğde, Turkey
- <sup>ar</sup>Forschungszentrum Jülich, Institut für Kernphysik, D-52425 Jülich, Germany
- <sup>as</sup>Physik-Department E12, Technische Universität München, D-85748 Garching, Germany
- <sup>at</sup>Faculty of Physics, Warsaw University of Technology, ul. Koszykowa 75, 00-662 Warszawa, Poland
- <sup>au</sup>Heavy Ion Laboratory, University of Warsaw, ul. Pasteura 5A, 02-093 Warszawa, Poland
- <sup>av</sup>Department of Physics, University of Jyväskylä, P.O. Box 35, FI-40014, Finland
- <sup>aw</sup>Fundamental Physics, Chalmers University of Technology, S-412 96 Gothenburg, Sweden
- <sup>ax</sup>Instituto de Estructura de la Materia - CSIC, E-28006 Madrid, Spain
- <sup>ay</sup>Department of Physics, University of Surrey, Guildford, GU2 7XH, UK
- <sup>az</sup>Faculty of Physics, St. Kliment Ohridski University of Sofia, Bulgaria
- <sup>ba</sup>Istanbul Technical University, Istanbul, Turkey
- <sup>bb</sup>Department of Physics, Lund University, SE-22100 Lund, Sweden

---

## Abstract

The Advanced GAMMA Tracking Array (AGATA) is a European project to develop and operate the next generation  $\gamma$ -ray spectrometer. AGATA is based on the technique of  $\gamma$ -ray energy tracking in electrically segmented high-purity germanium crystals. This technique requires the accurate determination of the energy, time and position of every interaction as a  $\gamma$  ray deposits its energy within the detector volume. Reconstruction of the full interaction path results in a detector with very high efficiency and excellent spectral response. The realization of  $\gamma$ -ray tracking and AGATA is a result of many technical advances. These include the development of encapsulated highly-segmented germanium detectors assembled in a triple cluster detector cryostat, an electronics system with fast digital sampling and a data acquisition system to process the data at a high rate. The full characterization of the crystals was measured and compared with detector-response simulations. This enabled pulse-shape analysis algorithms, to extract energy, time and position, to be employed. In addition, tracking algorithms for event reconstruction were developed. The first phase of AGATA is now complete and operational in its first physics campaign. In the future AGATA will be moved between laboratories in Europe and operated in a series of campaigns to take advantage of the different beams and facilities available to maximize its science output. The paper reviews all the achievements made in the AGATA project including all the necessary infrastructure to operate and support the spectrometer.

**Keywords:** AGATA, Gamma-ray spectroscopy, Gamma-ray tracking, HPGe detectors, Digital signal processing, Pulse-shape and gamma-ray tracking algorithms, Semiconductor detector performance and simulations  
**PACS:** 07.50.Qx, 07.85.Nc, 29.30.Kv, 29.40.Gx, 29.40.Wk, 29.85.Ca, 29.85.Fj

## 1. Introduction

Contemporary nuclear physics research aims at understanding the microscopic and mesoscopic features of the nuclear many-body system, determined by the effective interactions and underlying symmetries. These aims are often addressed by studying the nuclear system under extreme values of isospin, mass, angular momentum or temperature. In particular many facets of the nuclear system can be probed and understood by studying nuclei far from stability. With the inception of the new generation of Radioactive Ion Beam (RIB) facilities, in the case of Europe FAIR (Darmstadt, Germany), HIE-ISOLDE (CERN, Geneva, Switzerland), SPIRAL2 (Caen, France) and SPES (Legnaro, Italy), where a much wider range of unstable proton- and neutron-rich nuclei will become accessible, a new era is being opened for nuclear physics experiments.

For five decades, high resolution  $\gamma$ -ray spectroscopy, in particular with the large germanium detector arrays, has become a cornerstone in nuclear structure studies. Intense research and development efforts during the 1980's and the 1990's both in Europe and in the USA led to the construction of efficient  $4\pi$  escape-suppressed  $\gamma$ -ray spectrometers [1, 2]. Although the escape-suppression technique significantly improves the peak-to-total ratio in  $\gamma$ -ray spectra, it limits the solid angle occupied by the germanium detectors and therefore the efficiency of the  $\gamma$ -ray detection system. This detection technique culminated with the design and construction of the EUROBALL [3, 4] and GAMMASPHERE [5] spectrometers in Europe and in the USA, respectively. This contributed in a significant way to the impressive progress made in nuclear structure research since then.

In recent years, new important technical advances, namely that of position sensitive Ge crystals and tracking array technology, were developed to cope with Doppler effects due to large source velocities and the experimental conditions at the future facilities for intense radioactive and high-intensity stable ion beams. These conditions are expected to be extremely challenging, requiring unprecedented levels of sensitivity and count-rate capabilities. The required performance figures are beyond reach with conventional escape-suppressed arrays. The use of electrically segmented Ge crystals enables the identification of the individual points of interaction of the  $\gamma$  rays within the volume of the Ge crystals as well as the determination of the deposited energy with high resolution. Besides the highly-segmented Ge detectors, the realisation of such an array requires digital sampling electronics to extract energy, time, and position information from the detectors' output signals us-

ing pulse-shape analysis methods. The path of the  $\gamma$  rays in the Ge crystals can then be reconstructed, making use of "tracking" algorithms on the position and energy information of the individual interactions, and the full energy of the original  $\gamma$  ray can be determined. With the  $\gamma$ -ray tracking technique [6, 7], the Compton-suppression shields become unnecessary resulting in a large gain in efficiency while maintaining spectral quality. Furthermore, the direction of emission of each individual  $\gamma$  ray can be determined with high precision, which is crucial for a good Doppler energy correction and hence to achieve a good energy resolution even when  $\gamma$  rays are emitted from a fast moving nucleus, as is the case in most nuclear reactions.

This radically new concept constitutes a dramatic advance in  $\gamma$ -ray detection that will have wide-ranging applications also in medical imaging, astrophysics, nuclear safeguards and radioactive-waste monitoring, as well as establish a new level of detection capability for nuclear-structure studies. Given the importance of this development and its far-reaching implications, a European collaboration currently consisting of over 40 institutions from 12 countries has been established to develop and construct a European  $4\pi$  tracking spectrometer called AGATA (Advanced GAMMA Tracking Array). A similar project, GRETINA/GRETA, is also ongoing in the USA [7, 8]. The development of a tracking spectrometer in Europe is based on progress made within many previous projects, e.g. MINIBALL [9, 10], MARS [11], some of which were co-ordinated and supported by the EU TMR programme (project title: Development of Gamma-Ray Tracking Detectors for  $4\pi$  Gamma-Ray Arrays) [12, 13].

AGATA is a mobile instrument that will move between major laboratories in Europe take advantage of the range of different beams and equipment at each laboratory and to optimize the use of beam time at these facilities. AGATA will therefore be operated in a series of science campaigns at specific European facilities. It is now fully operational in its first physics campaign at INFN Laboratori Nazionali di Legnaro (LNL) in Italy, utilizing the wide range of stable beams available. Subsequently it will operate at the GSI facility in Germany and the GANIL laboratory in France and later at new radioactive beams facilities such as FAIR, SPIRAL2, SPES and HIE-ISOLDE. The spectrometer will be expanded over time, in phases, towards the full  $4\pi$  180 detector system.

This paper describes concisely the AGATA spectrometer and summarizes all the necessary developments that have been performed by the AGATA collaboration for its design, construction and operation. These develop-

ments range from advances in Ge detector technology, digital data acquisition systems, signal decomposition and  $\gamma$ -ray interaction reconstruction, and in many areas of the infrastructure needed to support and operate such a complex device.

## 2. Conceptual design

The conceptual design of AGATA explored the possible configurations of a  $\gamma$ -ray tracking array and compared their performance in a consistent way. This process was described extensively in [14]. Here only the basic ideas and the most important results will be summarised.

It is evident that, in order to maximise the detection efficiency of AGATA, the solid angle coverage should be maximised. In addition, to minimise the development and maintenance costs, the solid angle should be covered with only a few elementary shapes. The passive parts of the array should be minimised by using composite detectors, implying grouping (clustering) more crystals within the same cryostat. Moreover, to simplify the handling and maintenance of such complex objects, the detectors should rely on the encapsulation technique originally developed for the EUROBALL Cluster detectors [15]. An additional requirement in the conceptual design of AGATA was to keep a sufficiently large inner space inside the array in order to host the foreseen complementary instrumentation, which often is indispensable in the physics programme of AGATA.

The most elegant way to achieve a large solid angle coverage with a few elementary shapes relies on a decomposition of the icosahedron, namely of the platonic polyhedron having the largest number of faces. Such a decomposition will always result in 12 regular pentagons and a variable number of irregular hexagons once projected onto the spherical surface. As discussed in more detail in [14], the configurations having 120 or 180 hexagons were soon identified as the most attractive ones for AGATA, given the possibility to cover the solid angle with a few crystal shapes (2 and 3 for the case of 120 and 180 hexagons, respectively) and to easily form clusters of crystals (one kind of cluster with 4 and 3 crystals for the case of 120 and 180 hexagons, respectively). The contribution to the overall detection efficiency provided by the 12 pentagonal detectors was considered too limited to justify the extra costs for development. Therefore, the geometry of the array was optimised by minimizing the size of the pentagons. Indeed, the pentagonal holes can be utilised for mechanical support, insertion of complementary detectors and for the beam entry and exit pipes.

The possible configurations for AGATA were evaluated through detailed Monte Carlo simulations of the full array. The simulation code for AGATA is based on the C++ classes of GEANT4 [16], which provide a full description of the microscopic interactions of radiation with matter, as well as tools to implement the geometry of complex detector arrangements and to process and extract the relevant information. The GEANT4 geometry libraries were complemented with a specific class capable of describing irregular convex polyhedral shapes as the AGATA elementary shapes.

Establishing the optimal geometrical configuration for AGATA was a complex problem where the ingredients considered went beyond the mere overall performance figures of the array and other factors such as the reliability, simplicity, symmetry and cost of the adopted solution were taken into account.

From the results of the Monte Carlo simulations described in [14], it can be concluded that the configuration with 180 hexagonal crystals (Fig. 1) has better energy resolution, full-energy efficiency (Fig. 2) and peak-to-total (P/T) ratio than any configuration based on 120 detectors in a broad range of experimental conditions. The difference in performance is particularly evident at high  $\gamma$ -ray multiplicity, see Fig. 3. The performance figures for 1 MeV photons of the final optimised geometry with 180 detectors are 82 % solid angle coverage, 43 % (28 %) full-energy efficiency and 59 % (43 %) P/T ratio at a photon multiplicity  $M_\gamma = 1$  ( $M_\gamma = 30$ ). The final configuration for AGATA was therefore chosen to be based on 180 segmented hexagonal crystals.

With hexagonally shaped crystals the azimuthal segmentation is quite naturally based on 6 sectors, each of them centred on the crystal corners. The pattern of the longitudinal segmentation was optimised on the basis of detailed electric field simulations. On one hand, the effective volume of the segments should be balanced. On the other hand, the number of longitudinal segments should be large enough to achieve the required position resolution after the pulse-shape analysis process, namely 5 mm FWHM as calculated in the Monte Carlo simulations. A longitudinal segmentation based on 6 “rings” was considered the best compromise between the required performance and the cost of the associated electronics. For further details regarding the crystal segmentation scheme, see subsection 3.1.

## 3. Detectors

The AGATA detectors are based on encapsulated and electrically segmented closed-end coaxial  $n$ -type high-purity germanium (HPGe) crystals. The crystals have a

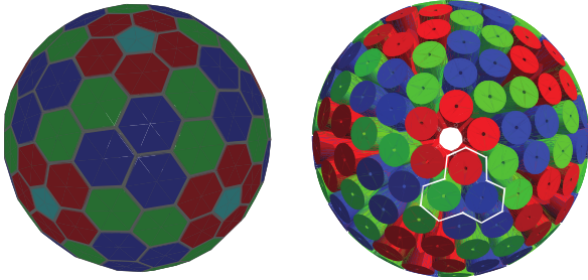


Figure 1: (Colour online) Computer aided design images of the tiling of the sphere (left) and the 180 crystal configuration (right). The cryostats and the detector encapsulation are not shown.

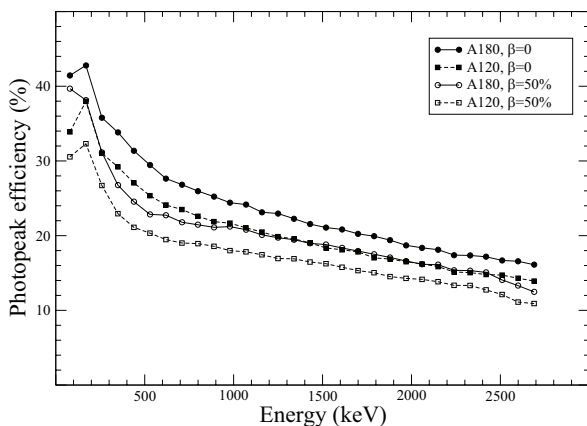


Figure 2: Simulated full-energy efficiency for the 120 crystals and the 180 crystals (AGATA) arrays as a function of the  $\gamma$ -ray energy and at multiplicity  $M_\gamma = 30$ , emitted by a point source recoiling along the  $z$  axis, with velocity  $v/c = 0$ , and  $v/c = 0.5$ .

tapered hexagonal geometry with an asymmetric shape to fit into the  $4\pi$  180 detector geometry (see Fig. 1). This geometry is realised with three different shapes, with a triplet of crystals arranged in identical triple cryostats, such that the full  $4\pi$  array has 60 cryostats. With this configuration, having a 9 cm thick germanium shell, a solid angle coverage of up to 82 % is realised. Its rather large inner radius of 22.5 cm (to the endcap face of the cryostat) allows the use of most ancillary detectors.

The AGATA triple cluster (ATC) detector contains three 36-fold segmented HPGe crystals. The total energy deposited in each crystal is collected in the central contact (core) leading to 37 signals per crystal. Therefore, the ATC detector contains 111 high-resolution spectroscopy channels. A more detailed description of the ATC detector is given in [17, 18]. All signal channels are equipped with a cold preamplifier stage operated close to the liquid nitrogen temperature of the

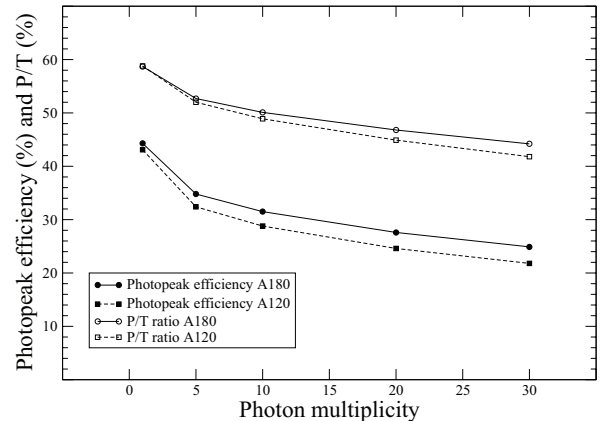


Figure 3: Simulated full-energy efficiency and peak-to-total (P/T) ratio for the 120 crystals and the 180 crystals (AGATA) array for 1 MeV photons as a function of the  $\gamma$ -ray multiplicity. The  $\gamma$  rays have been emitted by a stopped point-like source.

cryostat. The core preamplifier is characterised by low noise and a large dynamic range for energy detection, pulse-shape analysis and timing properties. A novel reset technique of the core preamplifier allows for an increased counting rate capability of the detectors of more than 50 kHz, preserving an energy resolution close to the nominal one. Moreover, the energy range of the ATC detector is substantially extended from 20 MeV to 180 MeV, see subsection 3.3. These developments are documented in [19–21]. Despite the high electronic integration density only small cross-talk contributions, typically less than 1 in  $10^{-3}$ , are measurable between the segments within a crystal. This cross-talk contribution is an expected effect caused by capacitive coupling of the signals via the bulk Ge material and can be well described within an electronic model of the combined crystal and preamplifier assembly [22, 23].

### 3.1. The AGATA crystals

All detectors are produced by the company Canberra, France. The three types of detectors employed in AGATA merely differ in their irregular hexagonal shape (see Fig. 4). The different geometries are assigned a letter and a colour: A – red, B – green and C – blue. A serial number is also assigned to each crystal (A001, A002, etc.). The crystals have a length of  $90 \pm 1$  mm and a diameter of  $80^{+0.7}_{-0.1}$  mm at the rear. At the front they are tapered to a hexagonal shape with a  $10^\circ$  tapering angle. The crystal's central hole has a diameter of 10 mm and extends to 13 mm from the front end. The 6-fold sector-wise segmentation goes through the middle of each flat hexagonal side. The 6-fold longitudinal segmentation

forms rings of 8, 13, 15, 18, 18 and 18 mm in thickness starting at the hexagonal front face of the crystal (see Fig. 4). The thicknesses of the rings have been optimised for a uniform distribution of the  $\gamma$ -ray interactions and optimal pulse-shape sensitivity [11]. The segment labelling scheme of the AGATA crystals is shown in Fig. 5.

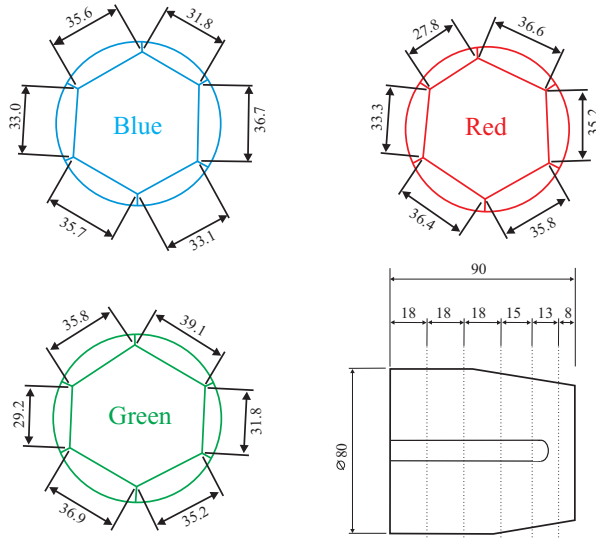


Figure 4: (Colour online) Drawing of the three AGATA crystal geometries. The AGATA triple cluster detector combines the three different crystal shapes. The side view (lower right) shows the position of the segmentation lines. All dimensions are given in mm.

The weight of a bare AGATA Ge crystal is about 2 kg. All crystals are made of *n*-type HPGe material with an impurity concentration specified to be between 0.4 and  $1.8 \times 10^{10} \text{ cm}^{-3}$ . The surfaces of these crystals are very delicate and therefore each crystal is encapsulated into a hermetically sealed aluminium canister with a 0.8 mm wall thickness (see Fig. 5). The encapsulation technology was developed for the EUROBALL cluster detectors [24] and extended to segmented detectors within the frame of the MINIBALL project [9]. The distance between capsule walls and crystal side faces is 0.4 mm to 0.7 mm. The 6×7 connector feed-throughs provide access to each of the 36 segmented outer contacts. The core contact, which is used for applying the high voltage and to obtain the core energy signal, is isolated with ceramic material. Efficient  $\gamma$ -ray tracking requires extreme care with the close packing of the crystals. The capsules are accurately mounted in the ATC detector with a 0.5 mm spacing between the flat surfaces.

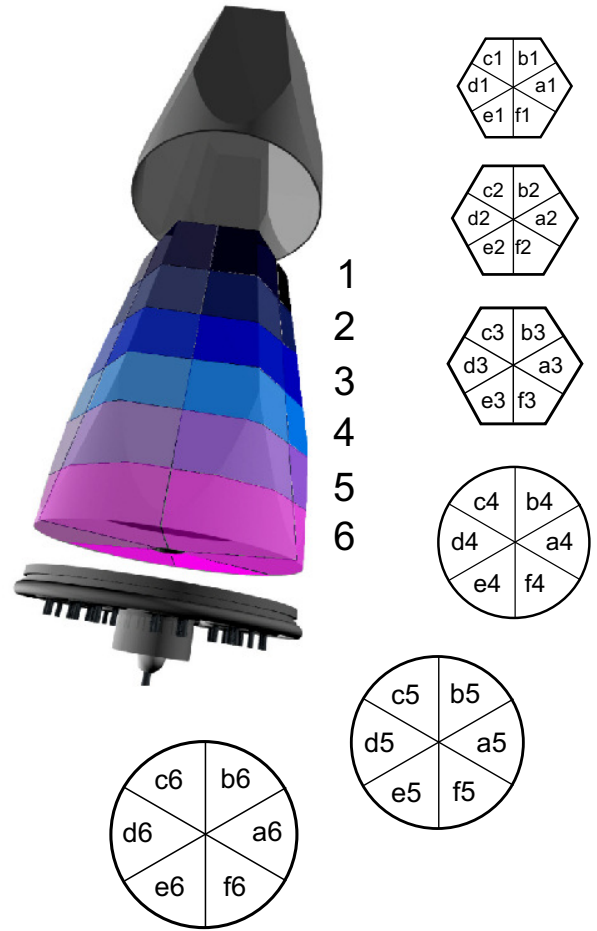


Figure 5: (Colour online) Segment labelling scheme of the AGATA HPGe capsules. Along the crystal axis the external contact is subdivided into six rings labelled 1 to 6. Each ring is subdivided into six sectors labelled a to f.

### 3.2. The AGATA cryostats

The cryostats of the ATC detectors were assembled and successfully commissioned in a common effort by the company CTT Montabaur, together with the AGATA collaboration.

The preamplifiers of segment and core contacts are divided in two spatially separated parts. The cold input stages of the preamplifiers are operated close to the Ge crystals. Cooling and mounting in close proximity to the detector is required to optimise noise performance. In addition a good electronic shielding between the input stages is required in order to minimise cross-talk effects. The AGATA cryostats employ a separated cooling scheme for the encapsulated Ge detector and the cold part of the preamplifier electronics. While the Ge detectors are cooled to 90 K, the FETs (Field Effect Tran-

sistors) are operated at temperatures near 130 K where their noise contribution is minimal. The other adjacent parts of the preamplifier electronics contribute less to the noise performance and are therefore situated outside the vacuum, where they are readily accessible. The electric connection between the two parts is made by several hundreds of individual thin wires with low thermal conductivity.

The thermal isolation is established by a vacuum with pressure values below  $1 \times 10^{-6}$  mbar. This pressure is maintained over long periods by the active getter materials built into the cryostat.

Although each individual FET has only an electric power consumption of  $\sim 20$  mW, the total consumption of the 111 FETs in one ATC detector adds up to 2.3 W. Together with the enhanced thermal connection by the wiring inside the cryostat and the radiative heat absorption, a considerable cooling capacity is demanded. The Dewar of the triple cryostat contains up to 4.5 l of liquid nitrogen. It has a length of 38 cm and an outer diameter of 25 cm. A full Dewar is sufficient for about 8 h of continuous operation. An electronic measurement of the liquid nitrogen filling level, which is based on a capacitance measurement between a metallic cylindrical tube inside the Dewar and the inner wall of the cryostat [18], is incorporated in the Dewar. The temperature is monitored by two platinum resistance thermometers of the type PT100, one attached to the copper cooling finger close to the Dewar and the other one positioned close to the crystals.

The triple cryostats have a length of 92 cm and a weight of 48 kg including the crystals and liquid nitrogen. Very tight tolerances are demanded for the manufacturing of the cryostat endcaps such that the final spacing between the endcap side faces of neighbouring triple cryostats is 0.5 mm. Fig. 6 shows 5 ATC detectors mounted into the support structure at LNL and demonstrates the challenges in the design, assembly and on-site installation of such cryostats.

### 3.3. Preamplifiers

The preamplifiers for the AGATA detectors require, besides the traditional good energy and timing properties, also fast and clean transfer functions to register unperturbed signal traces for pulse-shape analysis. In addition, a high count-rate capability was demanded in order to exploit fully the high geometrical efficiency. New preamplifiers have been developed by the AGATA collaboration which fulfill these requirements [19–21]. The segment and core signals of the AGATA detectors are read out through advanced charge-sensitive resistive feedback preamplifiers, employing a new fast-reset

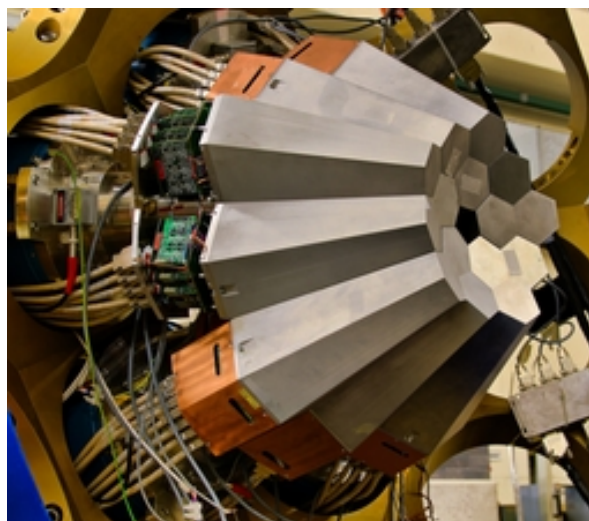


Figure 6: (Colour online) Photograph of the setup with five AGATA triple cluster detectors installed at LNL in Italy.

technique for dead time and dynamic range optimisation as well as an original circuit structure for maximising the open-loop gain of the charge-sensing stage.

The preamplifiers have a cold and a warm part. The cold part consists of a low-noise silicon FET, model BF862, a 1.0 pF feedback capacitance and a 1 G $\Omega$  feedback resistance. A dedicated shielding was developed for the cold preamplifier board for minimising the inter-channel cross talk. The warm part, operated at room temperature, is separated by 15 cm cabling inside the vacuum from the cold part of the cryostat and comprises a low-noise transimpedance amplifier, a pole-zero stage, a differential output buffer, and fast-reset circuitry.

The core preamplifier [21] is characterised by low noise and a large dynamic range for energy detection, pulse-shape analysis and timing properties. Transient signals are not deformed due to the large bandwidth. The core preamplifier possesses high count-rate capabilities and an embedded precision pulser.

The fast reset is provided by the desaturation circuitry, which is capable of detecting saturated signals. In such a situation a current source is connected, discharging the capacitance in the pole-zero network and achieving a fast restoration of the output level.

This innovative time-over-threshold (TOT) technique [20] for high-resolution spectroscopy extends the  $\gamma$ -ray energy range up to about 180 MeV. In this technique the energy is obtained through a precise determination of the reset time, required by the desaturation circuitry, which is measured as a time difference. The time measurement is started when the electronic pulse exceeds

the saturation threshold and is stopped when the pulse amplitude becomes smaller than this threshold. The time difference is strictly related to the pulse height of the saturating energy signal and allows an energy determination with a good energy resolution (FWHM) of about 0.2 %. This TOT energy resolution value can be compared for energies around 10 MeV with values of about 0.15 % achieved by the standard pulse height mode. Beyond 10 MeV the FWHM values are even comparable in both modes.

A custom programmable high-precision pulser is located on the core-preamplifier board. Its applications are: testing, calibration, time alignment and dead-time corrections, which are relevant for efficiency measurements of the detector. The pulser is used to inject calibration pulses to the core electrode itself as well as to all segment electrodes through the detector bulk capacitance. The output signal of the pulser is DC coupled to the source pin of the core input FET through a resistor divider consisting of a 48.5  $\Omega$  resistor and a grounded 1.8  $\Omega$  resistor. Thereafter the signal reaches each of the 36 detector segments via the capacitive coupling of the core to the segments.

A detailed description of the newly developed segment preamplifiers is given in [21]. Three segment preamplifier channels are integrated on one printed circuit board. The power consumption per segment channel is limited to 350 mW allowing the 108 closely packed spectroscopic channels to be operated close to the vacuum feed-throughs in air.

Differential signal outputs of the 111 spectroscopic channels are transmitted through 21 MDR (Mini D Ribbon) high-speed digital data-transmission cables. The segment MDR connectors merge the 6 segment signals of each sector. The core preamplifier has an individual MDR connector for the preamplifier output signal and the pulser control signals. Table 3 of ref. [17] summarises the most relevant specifications and their values.

### 3.4. AGATA detector specifications

The individual AGATA detectors have to meet the detector specifications given by the collaboration. The core energy resolution (FWHM) is specified to be better or equal to 2.35 keV (1.35 keV) at 1.33 MeV (122 keV) and the peak shape FWTM/FWHM (FWTM = full width at tenth maximum) is smaller than 2.00. The segment FWHM at 1.33 MeV (60 keV) is specified to be better or equal to 2.30 keV (1.30 keV) with a mean value of the 36 segments values better or equal to 2.10 keV (1.20 keV). The cross talk between channels has to be smaller than  $1 \times 10^{-3}$ . Upon delivery, the

specifications are verified during a customer acceptance test, which is performed by the AGATA collaboration at three sites, IKP Cologne, University of Liverpool and CEA Saclay. For these measurements single test cryostats are used, which are equipped with 37 cold input stages. Typically standard analogue commercial electronics is used for energy-resolution measurements. The cross-talk properties are determined with a 37 channel coincidence electronics based on high-speed digital sampling electronics. They are extracted from a  $^{60}\text{Co}$  measurement after adding the coincident signals of any pair of segments as the variation of the 1332.5 keV full-energy peak position. The peak shift should not exceed 0.65 keV. The most relevant parts of the specifications are summarised in detail in Table 1 of ref. [17].

### 3.5. Performance of the AGATA triple cluster detector

The ATC detector is equipped with three single core preamplifier boards and  $3 \times 12$  triple segment preamplifier boards. Energy resolutions at 60 keV for all segments and at 122 keV for the cores, are measured with analogue electronics. At higher energies (1332.5 keV), the measurements are performed also with digital electronics. The results obtained with a triple cryostat are compared in Fig. 7 at low energy and in Fig. 8 at high energy with the measured performance of the same crystals in a single test cryostat. Average values of the energy resolution measurements for the first five ATC detectors are summarised in Tables 1 and 2.

The values obtained for the segments in the triple configuration are on average even better than in the single test cryostat. Since these resolutions are dominated by electronic noise, it demonstrates the successful design and integration of the new AGATA triple cluster detector. Especially the electronic properties comprising the cold and warm parts of the new AGATA preamplifier assembly is causing very low noise contributions in the triple cryostat despite the high integration density of 111 analogue channels. In addition, an improved grounding was applied as a result of various iterations during the project. This reduces unwanted high-frequency and noise components and brings the energy resolution of the ATC detector at low energy to a value well within the specification.

The cross-talk contributions were investigated by analysing the coincident traces over a 7  $\mu\text{s}$ -long time period using the digital acquisition system on all three detectors. After identification of the true energy deposition in exactly one segment the coincident and simultaneous baseline shifts, which occur in all remaining 107 nonhit segments, are recorded for these one-fold events.



Table 1: Energy resolution values for the first five triple cluster detectors measured with analogue electronics at IKP Cologne. The core FWHM values were measured at 122 keV. The segment's average values and their standard deviations were measured at 60 keV. Not all the measurements were performed for ATC5.

Detector	Crystal	Core FWHM [keV]		Segment average FWHM [keV]	
		Single cryostat	Triple cryostat	Single cryostat	Triple cryostat
ATC1	A001	1.34	1.44	$1.08 \pm 0.07$	$1.01 \pm 0.05$
	B002	1.29	1.41	$1.09 \pm 0.09$	$1.04 \pm 0.07$
	C002	1.28	1.21	$1.03 \pm 0.08$	$0.97 \pm 0.06$
ATC2	A003	1.22	1.42	$1.14 \pm 0.08$	$1.05 \pm 0.07$
	B003	1.28	1.36	$1.06 \pm 0.07$	$1.00 \pm 0.07$
	C005	1.24	1.49	$1.16 \pm 0.07$	$1.14 \pm 0.11$
ATC3	A002	1.26	1.44	$1.03 \pm 0.08$	$0.93 \pm 0.11$
	B005	1.08	1.43	$1.05 \pm 0.08$	$1.05 \pm 0.08$
	C006	1.09	1.42	$1.15 \pm 0.10$	$1.14 \pm 0.11$
ATC4	A005	1.23	1.28	$1.04 \pm 0.09$	$1.11 \pm 0.17$
	B001	1.29	1.27	$1.02 \pm 0.07$	$1.03 \pm 0.10$
	C003	1.16	1.33	$1.00 \pm 0.09$	$1.11 \pm 0.38$
ATC5	A004	1.27	1.21	$1.17 \pm 0.08$	
	B009	1.36	1.54	$1.11 \pm 0.07$	$1.05 \pm 0.11$
	C004	1.30		$1.11 \pm 0.08$	

Table 2: Energy resolution values (FWHM) at 1332.5 keV for the first five AGATA triple cluster detectors. The single cryostat measurements were performed at IKP Cologne with analogue electronics as was the measurements marked ATC Cologne. The measurements at LNL were performed with the ATC detectors mounted on the frame using the AGATA digital electronics and data acquisition system. Average values and their standard deviations are given for the segments. Not all the measurements were performed for ATC5 at Cologne.

Detector	Crystal	Core FWHM [keV]			Segment average FWHM [keV]		
		Single cryostat	ATC at Cologne	ATC at LNL	Single cryostat	ATC at Cologne	ATC at LNL
ATC1	A001	2.33	2.46	2.50	$2.09 \pm 0.16$	$2.19 \pm 0.10$	$2.01 \pm 0.13$
	B002	2.27	2.46	2.43	$2.13 \pm 0.11$	$2.10 \pm 0.14$	$1.99 \pm 0.09$
	C002	2.25	2.33	2.42	$2.03 \pm 0.12$	$2.11 \pm 0.12$	$1.94 \pm 0.11$
ATC2	A003	2.28	2.41	2.56	$2.10 \pm 0.13$	$2.06 \pm 0.08$	$2.06 \pm 0.10$
	B003	2.23	2.52	2.42	$2.08 \pm 0.11$	$2.02 \pm 0.09$	$1.94 \pm 0.08$
	C005	2.20	2.21	2.39	$2.21 \pm 0.09$	$2.21 \pm 0.08$	$2.08 \pm 0.11$
ATC3	A002	2.31	2.40	2.52	$2.07 \pm 0.11$	$2.02 \pm 0.09$	$1.98 \pm 0.09$
	B005	2.29	2.42	2.49	$2.09 \pm 0.14$	$2.13 \pm 0.11$	$2.04 \pm 0.13$
	C006	2.16	2.27	2.58	$2.12 \pm 0.09$	$2.09 \pm 0.09$	$2.13 \pm 0.15$
ATC4	A005	2.23	2.40	2.19	$2.03 \pm 0.10$	$2.08 \pm 0.13$	$1.91 \pm 0.11$
	B001	2.17	2.50	2.30	$2.06 \pm 0.11$	$2.04 \pm 0.11$	$1.91 \pm 0.11$
	C003	2.34	2.35	2.40	$2.08 \pm 0.11$	$2.08 \pm 0.09$	$2.04 \pm 0.21$
ATC5	A004	2.31	2.36	2.33	$2.10 \pm 0.11$		$2.04 \pm 0.12$
	B009	2.33	2.49	2.63	$2.03 \pm 0.14$		$1.96 \pm 0.14$
	C004	2.23		2.26	$2.17 \pm 0.10$		$2.04 \pm 0.24$

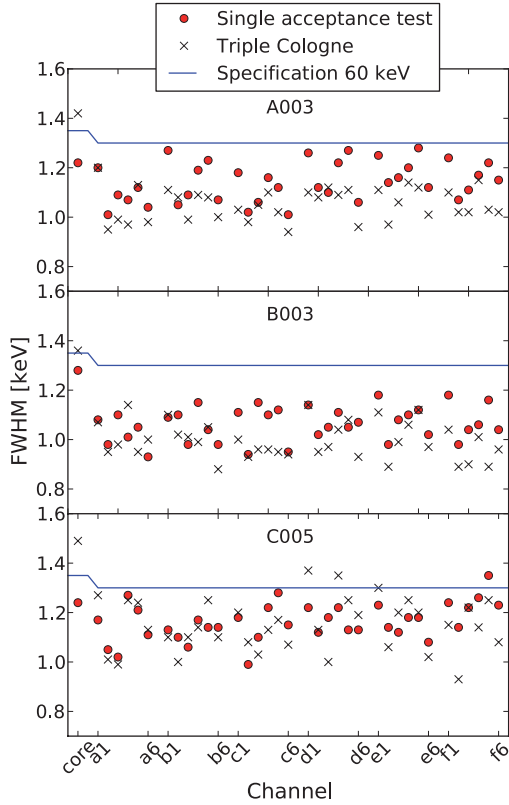


Figure 7: (Colour online) Energy resolution values of the crystals A003, B003 and C005 for the core signals at  $E_\gamma = 122$  keV and for the segment signals at  $E_\gamma = 60$  keV. The measurements were done at IKP Cologne using standard analogue electronics. The filled circles are the results of measurements performed with the crystals mounted in a single test cryostat while the crosses show measurements performed with the crystals mounted in a triple cluster detector (ATC2). The specification limits at 122 keV and 60 keV are shown as solid lines.

The correlation between the energy deposition in a single detector segment and the energy shift in all other segments is determined over an energy range given by  $\gamma$ -ray emission from  $^{60}\text{Co}$  and  $^{137}\text{Cs}$  sources. The observed cross talk is within the specifications and cross-talk contributions are only observed for segment combinations within the same detector crystal. The regular pattern is mainly caused by the different capacitances between the core and segment electrodes. A subset of  $105 \times 105$  combinations is shown in Fig 9.

The method applied to quantify this result is based on all possible combinations, shown in Fig. 9 for an ATC detector with the  $110 \times 111$  possible cross-talk matrix elements within the full triple cryostat. The cross-talk contributions between segments of different detectors are on the  $10^{-4}$  to  $10^{-5}$  level, which is well within the acceptable limits and which can be disregarded for

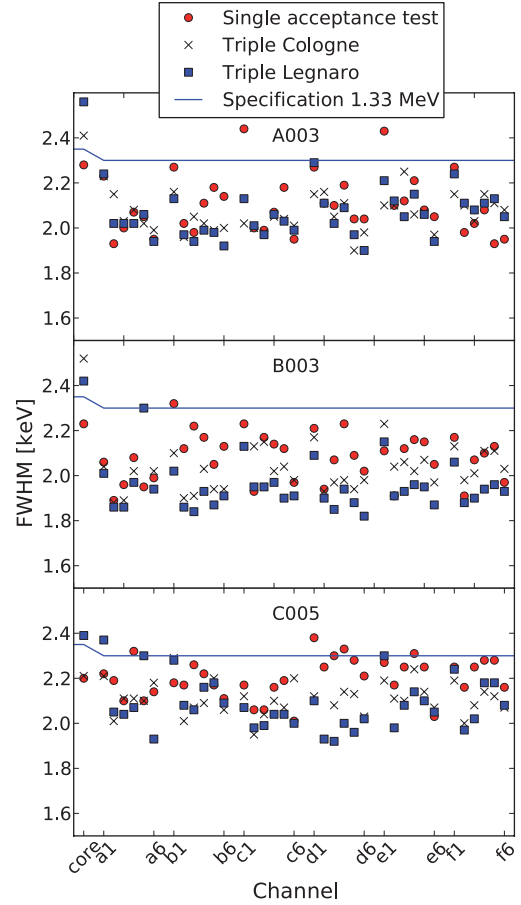


Figure 8: (Colour online) Energy resolution values of the crystals A003, B003 and C005 for the core and segment signals at  $E_\gamma = 1332.5$  keV. The filled circles and crosses show results of measurements performed at IKP Cologne using standard analogue electronics and with the crystals mounted in a single test cryostat and in a triple cryostat (ATC2), respectively. The filled squares show results of measurements performed at LNL with ATC2 mounted on the frame and by using the AGATA digital electronics and data acquisition system. The energy specification limit at 1332.5 keV is shown as a solid line.

a standard operation of the ATC detector.

The new method to determine precise and absolute cross-talk matrix elements was applied to all available AGATA triple detectors. The cross-talk pattern was measured to be at the 0.1 % level, comparable with the values shown in Fig 9. The observed structure can be entirely attributed to the capacitive coupling between core and segments via the bulk Ge material. This behavior is well reproduced by a linear electronic model. This cross-talk contribution is considered as the inherent cross-talk limit given by the construction of the new detectors [23]. The calculated values are closely approached by the obtained results. The cross-talk contributions in all AGATA detectors behaved very similarly,

implying that the development of the AGATA cryostats and the preamplifier electronics has progressed in such a way that the fundamental constraints are accounted for, detectable and understood.

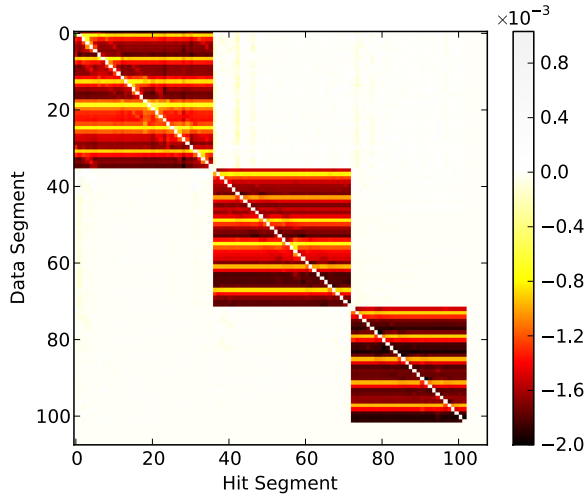


Figure 9: (Colour online) Observed relative cross-talk contributions of nearly all segment combinations between the three crystals of the ATC2 detector are plotted (only 105 channels were operational at the time of the measurement). The colour scale gives the relative cross talk in units of  $10^{-3}$ . A relative energy shift on the  $\sim 10^{-3}$  level is caused by cross talk for segment combinations within one of the three detectors. Cross talk between the three different detector capsules is observed to be negligible. The other tested ATC detectors show similar results.

#### 4. Detector characterisation

The success of the AGATA project relies on the ability to reconstruct the trajectories of  $\gamma$  rays scattered within the germanium detectors. The deposited energy and the location of the photon interactions can be extracted from the measurement and the analysis of the waveforms that arise on the segments during the charge collection. The pulse-shape analysis algorithms currently developed use databases of calculated pulse shapes. These calculated pulses need to be validated with real pulse shapes taken at various points within a detector. For the development of tracking algorithms, it is also crucial to determine experimentally the interaction position sensitivity in three dimensions in the whole volume of a detector.

The AGATA collaboration has performed a detailed analysis of the response function of the crystals. This work included developing a theoretical basis data set, which describes the detector response function and then validating this against the equivalent experimental data.

Such knowledge provides the project with the information necessary to enable pulse-shape analysis and  $\gamma$ -ray tracking.

The AGATA collaboration has two operational experimental characterisation centres, based at the University of Liverpool in the UK and at CSNSM Orsay in France. Three new centres are being commissioned at GSI Darmstadt in Germany, at IPHC Strasbourg in France and at the University of Salamanca in Spain. This would significantly increase the number of AGATA detectors that could be experimentally characterized.

##### 4.1. Liverpool scanning system

A schematic diagram outlining the University of Liverpool AGATA detector scanning system is shown in Fig. 10 [25]. The figure displays the mechanical configuration of the system, with the detector vertically mounted above the collimated source assembly. A 920 MBq  $^{137}\text{Cs}$  source is mounted at the end of a 1 mm diameter coaxial tungsten collimator of 120 mm in length. The collimator is mounted in a lead collar and source housing assembly, which shields the system operators from the mounted source. The whole assembly is mounted on a precision Parker  $x$ - $y$  positioning table. The table is moved in precise computer-controlled steps through the use of Pacific Scientific stepper motors and two Parker Automation axis indexers. The system has a position accuracy of  $100\ \mu\text{m}$  and can scan over an area of the size  $30\ \text{cm} \times 30\ \text{cm}$ .

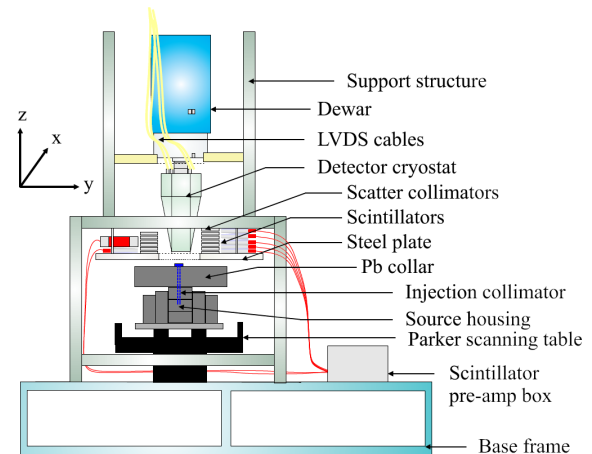


Figure 10: (Colour online) Schematic diagram of the University of Liverpool scanning table assembly.

A steel frame is constructed around the scanning table. From this, a steel plate is suspended by threaded

rods, on which the scatter collimators and scatter detectors can be supported. The rods enable the plate, and hence the collimators, to be moved in the  $z$ -direction. The steel plate has a square cut from its centre and is positioned to a height just above the lead collar. The AGATA detector is then inserted into the frame and positioned in the centre of the plate.

The experimental preamplifier pulse shapes observed as a function of the interaction position of a beam of  $\gamma$  rays can be recorded. The signals are digitized by utilizing either the GRT4 VME modules [26], which sample the signal with an 80 MHz frequency over a 14-bit dynamic range, or the GRETINA VME digitizer modules, which have a 100 MHz sampling frequency and the same 14-bit dynamic range. Both digitizer systems utilize an external trigger provided by the core-energy signal from the AGATA detector. Data is read out and recorded simultaneously for all 37 channels from a single crystal.

Scan data can be collected in singles and coincidence modes. Singles data yields  $x$ - $y$  information on the interaction position of a  $\gamma$  ray. Such a measurement is relatively quick to perform; however, the  $z$ -position information has large uncertainties, as it is only defined by the segment size. Coincidence scanning utilizes Compton scattering to define a single interaction position in  $x$ - $y$ - $z$ . Such a methodology demands that the  $\gamma$  ray Compton scatters to an angle of about  $90^\circ$  in the germanium detector, depositing the remaining energy in coincidence in a collimated ring of scintillation detectors. This method is very precise but can result in a very slow procedure due to the low coincidence rate between the germanium detector and the scintillators. A full characterisation of a crystal with a grid of 1 mm takes 2-3 months. A detailed analysis of singles and coincidence data for the prototype AGATA symmetric detectors can be found in [27, 28].

An example of a  $^{137}\text{Cs}$  singles scan of the front face of crystal C001 is shown in Fig. 11. Data were recorded on a 1 mm grid for 1 min at each position. The system was triggered externally with a low-energy threshold of  $\sim 650$  keV on the core contact in order to eliminate unwanted Compton scattered or background events. The resulting distributions of the intensity of 662 keV full-energy depositions confined to a single segment in rings 1 and 3 are shown in Fig. 11. The  $x$  and  $y$  axes represent the position of the scanning table in a range of  $\pm 40$  mm. The plots clearly show the segmentation pattern of the detector and the presence of the coaxial hole in ring 3.

The distributions of the  $T_{30}$  (10% to 30% of the maximum amplitude) and  $T_{90}$  (10% to 90%) rise times of the core signal are plotted in Fig. 12. In a coax-

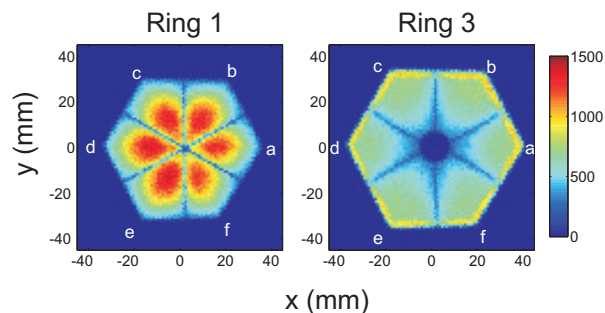


Figure 11: (Colour online) Distribution of the intensity of 662 keV full-energy depositions confined to a single segment in rings 1 and 3 of crystal C001. The colour scale gives the number of counts in the 662 keV peak recorded in 1 min.

ial  $n$ -type crystal, such as those used in AGATA, the  $T_{30}$  distribution is dominated by the drift time of the electrons towards the core contact, while the  $T_{90}$  distribution is determined by both the electron and the hole transport. As a result,  $T_{30}$  is expected to increase as the interaction point is moved from the core contact to the outer electrode, while a minimum value for  $T_{90}$  is expected at the locations in which the electron and hole collection times are equal. This behaviour is confirmed by the plots shown in Fig. 12. In ring 3,  $T_{30}$  ranges from  $\sim 30$  ns for small radii to  $\sim 100$  ns for large radii, while  $T_{90}$  ranges from  $\sim 100$  ns to  $\sim 240$  ns. For ring 1 (front ring of the crystal) both the  $T_{30}$  and  $T_{90}$  distributions have a different character due to the more complex electric field distribution in this region of the detector. Minimum rise times are observed at small radii due to the quasi-planar nature of the electric field leading to short charge collection times through the 13 mm distance from the front face to the hole drill depth in the crystal. These plots also show the influence of the face-centred cubic lattice orientation of the Ge crystal on the rise times. For pulses measured at the same radius, a maximum variation of 30% with respect to the crystal axes is observed for the time required to collect the charge carriers. This effect must be taken into account in the theoretical simulation, if a reliable validation is to be achieved.

The coincidence between an AGATA detector and an array of scintillator crystals can be used to select interactions at a specific location within the crystals. In practice, several events for each location are needed in order to average the corresponding waveforms and eliminate, as much as possible, the effects of the noise. The averaging procedure, performed for each location, starts with a scaling of each waveform by pre-calculated gain fac-

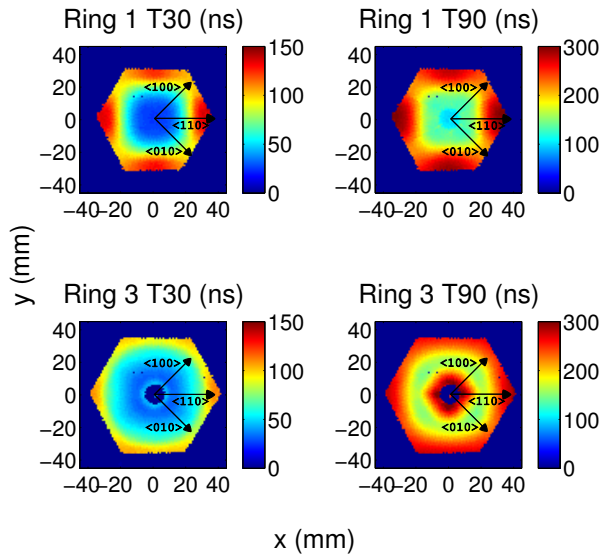


Figure 12: (Colour online) [Left] The distribution of the  $T_{30}$  (10-30%) rise time of the core signal for 662 keV full-energy depositions confined to a single segment in ring 1 (top) and 3 (bottom) of crystal C001. [Right] The corresponding  $T_{90}$  (10-90%) distribution. The crystallographic axes are illustrated. The colour scale gives the rise time in ns.

tors, derived from the  $^{152}\text{Eu}$  baseline difference energy calibration, and with a baseline subtraction. The baseline is derived for each individual trace from an average of the initial 10 samples in each trace.

Waveforms are then interpolated to allow for more accurate time alignment. The pulse amplitudes are subsequently normalized in order to have the same maximum amplitude for all of them. Finally, the best fit average waveforms corresponding to each location are obtained through a  $\chi^2$  minimisation procedure. Only the central contact, the segment with net charge deposition and its neighbours are considered in the fit. “Noisy” events which give a large  $\chi^2$  contribution are excluded from the fit procedure. The final result is exemplified in Fig. 13, where the average (thick red line) and the constituent (thin blue lines) pulse shapes are shown for a net charge deposition in segment c3. The effect of the cancellation of the random noise across the pulses is clearly visible. The standard deviation of the baseline noise for the average pulses is 0.9 keV, as opposed to 4.7 keV for single pulses. The pulse shapes illustrated in Fig. 13 also demonstrate the signal induced on the neighbouring segments b3, c2, c4 and d3. These transient signals are those induced on adjacent electrodes to the primary interaction due to the drift of the charge carriers inside the germanium crystal.

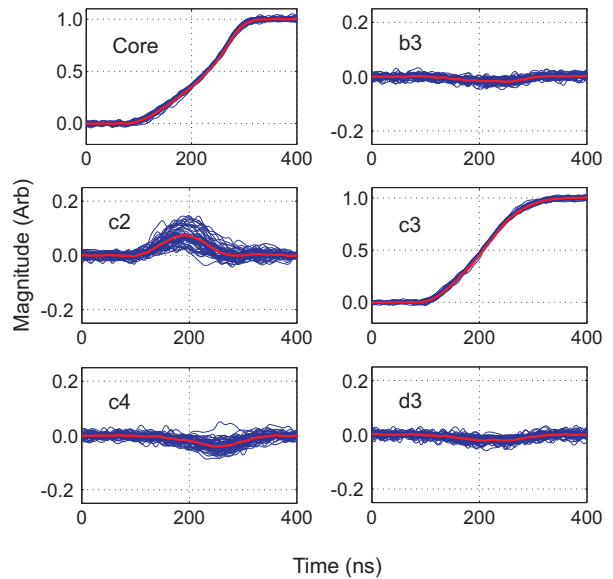


Figure 13: (Colour online) Average (thick red line) and all constituent (thin blue lines) pulse shapes for a typical interaction in segment c3 following the  $\chi^2$  rejection (see text). The signal induced in the core and in the neighbouring segments b3, c2, c4 and d3 are also shown.

#### 4.2. Orsay scanning system

The Orsay scanning system is based on the same concept as the Liverpool system, i.e. a well collimated strong radioactive source, an accurate moving system and an array of scintillator detectors to define the  $z$  position of the scattering through coincidence measurements. The main difference is that the  $z$  coordinate can be continuously scanned due to the absence of the scatter collimators, which are replaced by special tungsten collimators described below.

A schematic view of the scanning setup based at CSNSM Orsay is shown in Fig. 14 [29]. A 477 MBq  $^{137}\text{Cs}$  source is encapsulated in a stainless steel cylindrical container with a diameter of 4 mm, a height of 6 mm and window thickness of 0.4 mm. This container is inserted into a collimator made of densimet (W-Ni-Fe alloy, density 18.5 g/cm<sup>3</sup>). The  $\gamma$  rays emitted by the source are collimated by a hole with a diameter of 1.6 mm and a length of 155 mm.

Six modules of the TOHR (TOmographe Haute Résolution) detector are used to perform the coincidence measurements. Each module is made of a stack of 80 tungsten plates with a triangular shape and a thickness of 200  $\mu\text{m}$ . These plates have 400  $\mu\text{m}$  diameter holes positioned on a hexagonal lattice and the geometry of each stack acts as a many slit collimator (about 8000 slits) with a focal distance of  $\sim 7$  cm. At the back of each stack

of plates, there is a NaI(Tl) crystal for the detection of  $\gamma$  rays. The six modules are positioned in a compact semi-circle at  $\pm 10.2^\circ$  from the horizontal plane around the AGATA detector, all having the same focal point in the germanium crystal. The position of the common focal point can be changed by translating the TOHR array or by turning the AGATA detector about its central axis; thus allowing for a full 3D scan of the AGATA detector. A more detailed description and measurements can be found in Ref. [30].

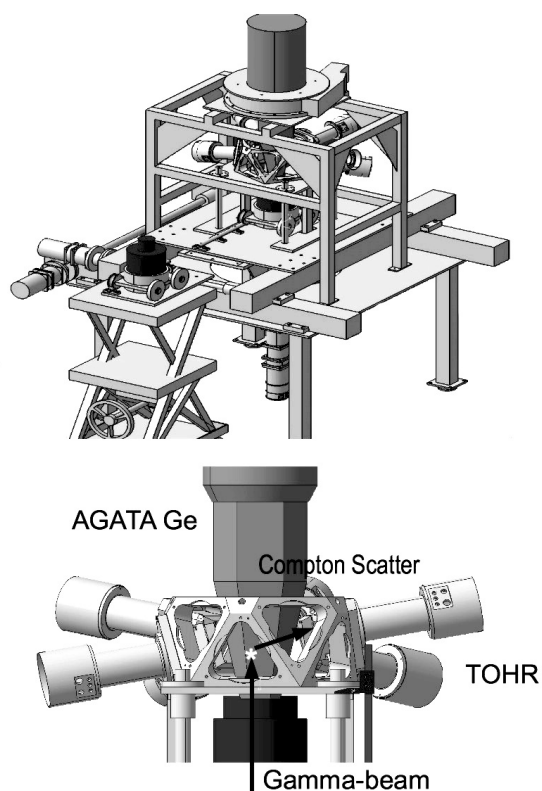


Figure 14: A schematic diagram showing the CSNSM Orsay scanning table assembly (top) and a closer view (bottom) showing the 6 NaI(Tl) detectors and the mechanical support for the TOHR, the AGATA detector and the collimated intense  $^{137}\text{Cs}$  source.

#### 4.3. Other scanning systems

Three additional scanning systems are under construction and validation within the AGATA collaboration. At the University of Salamanca a system, which is similar to the Liverpool and Orsay systems, is being developed, while different concepts of scanning are under validation in Strasbourg and at GSI. The technique used in Strasbourg is based on the pulse shape comparison scan (PSCS) principle [31]. In this setup the detector is

rotated instead of the source in order to scan the front and lateral sides of the entire germanium crystal with a collimated source of  $^{137}\text{Cs}$ .

A new characterisation method has been developed at GSI [32, 33]. This approach combines the PSCS principle with an advanced  $\gamma$ -ray imaging technique based on positron annihilation Compton scattering [34, 35]. The imaging is accomplished by means of a position-sensitive scintillation detector (PSD) [36] coupled to a  $^{22}\text{Na}$  source with an activity of 300 kBq. In order to reduce the background due to scattered  $\gamma$  rays, the  $^{22}\text{Na}$  source is placed in the centre of a tungsten collimator with two conical openings, one of which is oriented towards the germanium crystal, the other towards the PSD. The setup with the PSD, the source and the collimator can be rotated around a vertical axis at which the germanium crystal is located. Two measurements are typically carried out, in order to shine and image the entire crystal from two different sides. The PSD is operated in coincidence with the AGATA crystal. For each AGATA-PSD coincidence event, the traces from the core and all 36 segments are digitised and stored. The position of the  $\gamma$ -ray interaction in the PSD is also recorded. The latter allows for the 3D reconstruction of the trajectories of the two 511 keV annihilation quanta, which are assumed to be collinear. By applying the PSCS principle, the detector response for a particular  $\gamma$ -ray interaction point  $x$ - $y$ - $z$  in the AGATA crystal can be determined by comparison of the two data sets of pulse shapes, corresponding to the two scanned sides. The duration of a full scan of an AGATA detector on a 2 mm pitch grid will be strongly reduced compared to existing systems, down to about 10 days at Strasbourg and 3 days at GSI.

## 5. The AGATA infrastructure

The AGATA infrastructure includes the mechanical structure and all services to the detectors, mechanics, electronics and to the data acquisition system to ensure that spectrometer operates reliably. It includes the “life-support system” for the detectors providing the cryogenic cooling, the low- and high-voltage power supplies, constant monitoring, a user-friendly interface and reports on critical situations (detector warm up, power losses, etc.). This system is called the detector-support system (DSS).

### 5.1. The AGATA mechanics

AGATA requires a mechanical structure to accurately support the detector elements and enable their safe insertion and removal. The structure needs to be able to

locate the detectors accurately with minimal space between each ATC detector in order to maximise the solid angle coverage.

At LNL, AGATA is located at the target position of the PRISMA [37] magnetic spectrometer. The main design constraint imposed by PRISMA is that both AGATA and PRISMA must be free to rotate around the beam direction such that the optical axis of PRISMA ranges from  $0^\circ$  to  $117^\circ$ . Both AGATA and PRISMA are therefore mounted on a rotating platform that also supports the front-end electronics (digitisers), power supplies and autofill system. In addition, the arrangement at LNL allows the coupling to a range of ancillary detectors for specific measurements. This setup, including all the detector systems, is described in detail in Ref. [38].

The generic support structure for AGATA consists of a number of identical flanges (Fig. 15), one for each detector module. These are assembled together to produce a solid structure as shown in Fig. 16. This generic support structure is modular in concept and can be expanded up to the full  $4\pi$  system with 60 such flanges and will be used at all the host laboratories. The frame to support this structure will be different at each site because of the details of the location and the coupling to different spectrometers.

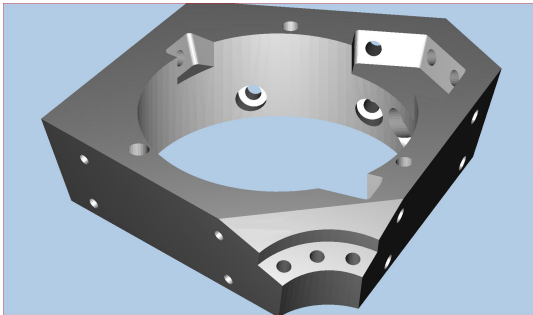


Figure 15: (Colour online) A computer aided design drawing of one of the main AGATA support flanges.

Accurate positioning of the detectors on the support structure is achieved by using a system of 3 precision sliding rods, one of which is threaded to enable controlled insertion and removal. The accuracy of this system was checked using a high-precision coordinate measuring machine. Under operational conditions the endcap underwent some deflection, which was modelled by finite element analysis (Fig. 17). An adjustment mechanism for the detector modules for each flange was therefore incorporated into the system. This adjustment mechanism comprises 3 rings to provide for the full 6 degrees of freedom adjustment. In addition, a stand-

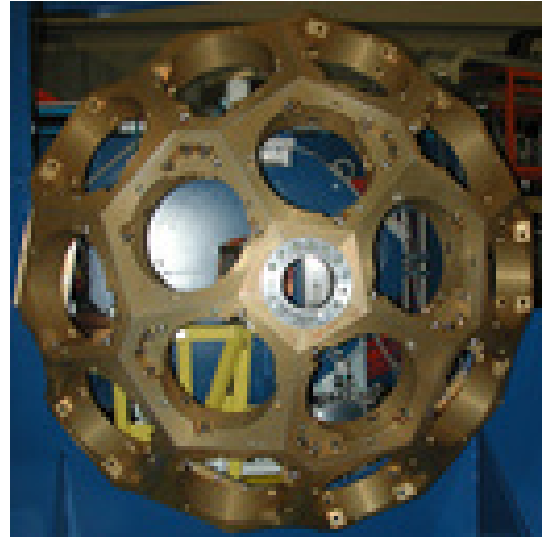


Figure 16: (Colour online) A photograph of 15 flanges mounted at LNL.

alone gauge was manufactured such that the detector module could be adjusted to its final orientation before mounting into the main support structure. The detector module needs to be positioned within 0.1 mm of its theoretical position, and so it was critical that this gauge was made to a high accuracy.

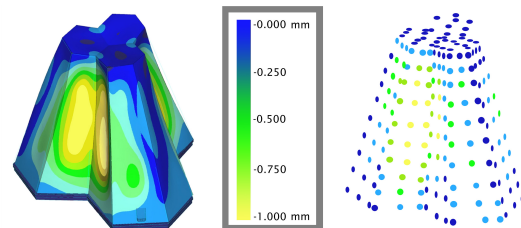


Figure 17: (Colour online) Right: measured endcap deflection of the detector module. Left: Finite element analysis deflection calculations of the endcap.

## 5.2. Detector-support system

The AGATA DSS consists of the low- and high-voltage power supplies, the autofill system and an uninterruptible power supply (UPS) system. The slow control of the DSS is managed by a system based on a programmable logic controller (PLC), which is accessed and controlled from a custom made graphical user interface.

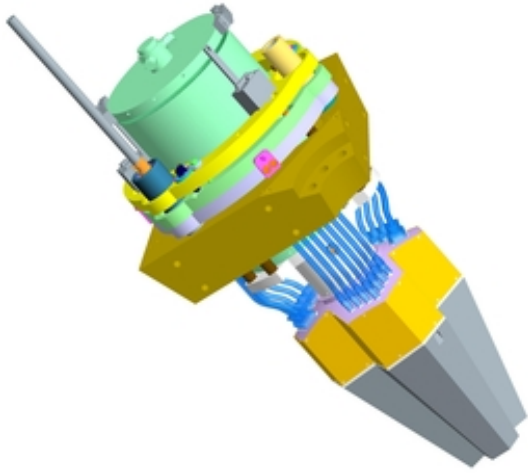


Figure 18: (Colour online) Computer aided design drawing of an ATC detector and the detector mounting arrangement comprising the main flange, 3 precision rods and the detector adjustment rings.

### 5.2.1. Low-voltage power supply unit

This unit supplies low voltage power to the preamplifiers, high-voltage modules, liquid nitrogen level measurement system, digitisers and to the PROFIBUS-DP (Decentralized Peripherals) field bus, which is used for controlling the power supplies.

The power consumption of the digitisers is much larger than of the other units. In order to reduce the noise pick-up, the digitisers are located as close to their power supplies as was practically feasible, at a distance of about 8 m. The preamplifiers, high-voltage modules and the liquid nitrogen level measurement systems are about 15 m from their related power supplies.

A low-voltage power supply from the company AXIS was chosen. It consists of a 4U crate (see Fig. 19), which contains all the needed power supplies:  $\pm 6$  V and  $\pm 12$  V for the preamplifiers,  $+6.5$  V for the high-voltage modules,  $\pm 12$  V for the liquid nitrogen level measurement system,  $+48$  V and  $+5$  V for the digitisers and  $+24$  V for the PROFIBUS-DP field bus. All power supplies are linear, including the  $+48$  V, which represents the most powerful module with a 1440 W load.

The design of the low voltage supply for the 111 preamplifiers uses a floating supply system, ensuring that the 0 V reference is at the detector itself and all return currents pass through the supply to minimise the overall detector noise. The preamplifier load is the highest on the  $+6$  V line and, to a lesser extent on the  $-6$  V line. The voltage drop across 15 m cable means that the  $+6$  V and  $-6$  V voltages have to be regulated at the load. This has been achieved to within a strict tolerance of  $\pm 0.05$  V.



Figure 19: (Colour online) The AXIS low-voltage power-supply unit generating  $\pm 6$  V and  $\pm 12$  V to power the 111 preamplifiers of the ATC detector,  $+48$  V and  $+5$  V for three digitisers,  $+6.5$  V for three HV Modules and  $+24$  V for the PROFIBUS-DP network.

### 5.2.2. High-voltage module

Presently, the high voltages for the ATC detectors are provided by a standard HV power supply produced by the company CAEN. A development is ongoing to equip each ATC detector with three HV modules, which will generate locally the  $\sim 5$  kV needed to bias the crystals; thus avoiding long HV cables and therefore reducing the pick-up noise. In this new design, the high voltages are filtered, controlled and monitored directly at the ATC detector. The high voltages are produced from a low voltage ( $+6.5$  V), which is provided by the AXIS unit.

Prototypes of the HV modules have been produced and they rely on a compact HV unit made by the company ISEG. The HV unit is able to communicate with the PLC via the PROFIBUS-DP field bus by using customised control electronics. Additionally, a microcontroller provides an autonomous bias shut down operation: each HV unit is able to initiate a bias shut down if the temperature of the detector or the current measured is too high. The bias shut down due to too high temperature is implemented by assigning one of the three HV modules of the ATC detector to act as a master and to read the PT100 temperature gauges of the detector. For security and maintenance reasons, several parameters are embedded in the microcontroller: the ID of the HV module, the serial number, the self-calibration values of the ISEG DC/DC converter, the maximum voltage, the maximum ramp-up and ramp-down voltage rates and the set threshold value for the current limit.

A photo of the prototype HV module is shown in Fig. 20.

### 5.2.3. Autofill system

The liquid nitrogen cooling of the ATC detectors is managed and monitored by the AGATA autofill system. This system provides information regarding the detec-



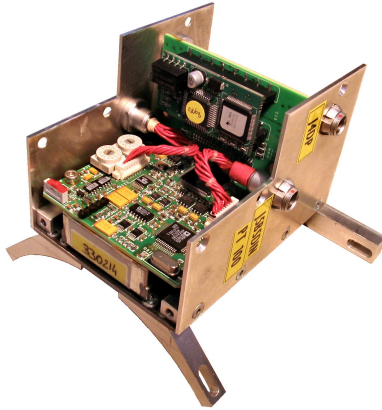


Figure 20: (Colour online) The AGATA high-voltage module composed of a compact ISEG DC/DC module and control-electronics boards including a microcontroller.

tor temperature and the amount of liquid nitrogen in the detector Dewar [18]. It controls the filling cycle and operates all associated valves.

The autofill system is based on a PLC driven process running under the PROFIBUS data acquisition and command standard. It performs the regular filling of the detectors, forces the filling of any detector if its temperature exceeds given threshold, issues warnings if any parameter declines from its regular values and issues alerts if any of the parameters is beyond the range of noncritical values. The system is able to manage a direct filling from a pipeline as well as via buffer tanks with the associated parameters, warnings and alarms. It can run in fully automatic mode, in semi-automatic mode (manual start of the fill but automatic follow up of the complete fill procedure; remote action using the graphical user interface of the GUI), in manual mode (full manual fill processed remotely using the graphical user interface of the DSS) and in local mode (manual fill of the detectors using keys on the autofill hardware in the experimental hall).

Technically the autofill hardware is made of the following components:

- A PLC which controls the autofill routine.
- A PROFIBUS crate, which contains the PROFIBUS terminals with various functions: PT100 readout, analogue readout (4 mA to 20 mA), digital input and output terminals, PROFIBUS watchdog, and the relevant power supplies. The signals from and the commands to the executors (valves, dialers) are sent via the valve control crate.

- A Valve control crate, which contains 4 valve control cards, one master card and one dry contacts board. The valve control crate is presently under development. Parts of its functionality are mimicked using a system based on relays in the present setup.

#### 5.2.4. Uninterruptable power supply

Many of the AGATA devices are protected by a UPS system. The power consumption of the digitisers is much larger than of the preamplifiers, which in turn is larger than the power consumption of the autofill system. In case of a power failure, the DSS determines when the power supply of each component is to be shut down and it initiates the power-off procedure. The goal of the DSS is to save enough power to enable a complete liquid nitrogen filling cycle.

#### 5.2.5. DSS slow control architecture

As reliability and safety of the DSS are of paramount concern, a PLC has been chosen to run the processes and to be the interface to the graphical user interface of the DSS. The PLC communicates with the different elements of the DSS (autofill, low-voltage power supply and high-voltage modules) via the PROFIBUS-DP field bus (Fig. 21).

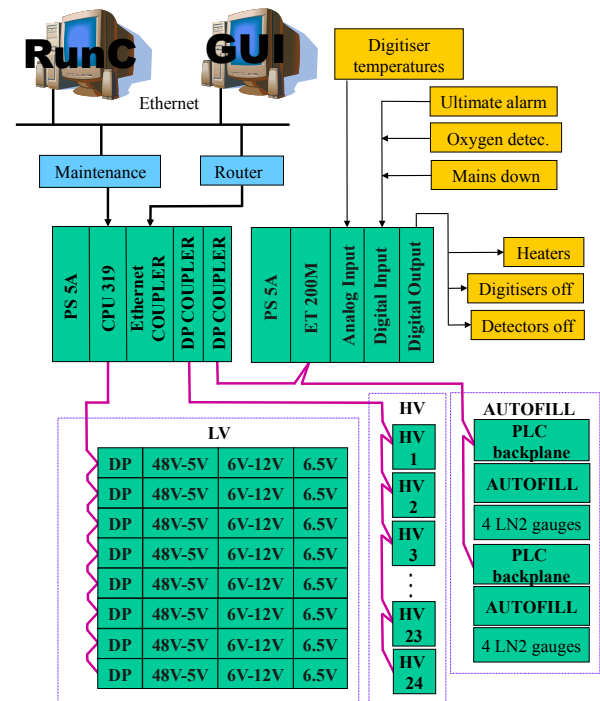


Figure 21: (Colour online) PLC architecture of the DSS. The PROFIBUS-DP field bus is indicated with red lines.

The communication between the PLC and the computer running the graphical user interface is performed through the use of an OPC (object linking and embedding for process control) server.

The maintenance server, which is based on an industrial PC, can be accessed remotely. It gathers all data concerning the particular process in order to be able to diagnose problems coming from the process itself, from the PLC or from the field bus.

### 5.2.6. Graphical user interface

The graphical user interface (GUI) of the DSS is designed to control and monitor the low voltages, high voltages and the autofill parts of the DSS. To ensure a user-friendly and easy-to-use interface, different requirements have been taken into account. Firstly, there are different groups of users that demand different kinds of information to be displayed and functions to be offered. Secondly, the amount of data to be displayed is quite large. Therefore, it is distributed among different display panels, such that only the relevant part is shown (Fig. 22). The DSS GUI offers various ways to access the whole set of data. For example, there are three tables showing all parameters for one detector, user selected parameters for all detectors or the raw data blocks from the PLC. A graphical representation of historical data can be displayed. The user can open multiple tabs and for each of them select the items to be displayed and updated periodically.



Figure 22: (Colour online) The graphical user interface of the AGATA detector-support system showing the autofill page. The autofill manages detectors in groups of 8 units. On the left hand side of the figure, the level of liquid in the main supply tank is shown as well as its internal pressure and the time remaining to the next programmed fill. On the right hand side, the colour of the detector endcap gives an indication of the detector temperature (blue for cold, orange for warming up, red for warm). Trending (real-time plot of any variable parameter), Control (parameter setting) and Alarms (alarm status) pages are also accessible from this GUI.

The object-oriented approach allowed the separation of the two main threads, the GUI and the PLC communication part. Both threads communicate with the DSS hardware interface, which holds all the data and manages the reading and writing from both sides.

### 5.3. Cable management

The management of the many cables required to service, control and extract signal information from the detectors is very important and has to be taken into account in the overall design. The type, length, weight and routing of cables has to be considered to enable detectors to be installed and extracted easily. The cabling management system will also be different at each host site.

### 5.4. Grounding and electromagnetic compatibility

To provide the best signal-to-noise ratio for the detector signals, especially for their use in pulse-shape analysis, grounding is of utmost importance. The design of the grounding includes the mechanics, the detectors and their preamplifiers, the digitisers and all hardware of the DSS. The rest of the AGATA system (pre-processing electronics and data acquisition system) is optically isolated from these front-end components.

It is mandatory that the AGATA grounding system shields the various components from both low- and high-frequency perturbations. Low-frequency disturbances ( $\sim 50$  Hz) cause energy resolution degradation in the detectors, but they are generally easy to filter out. High-frequency perturbations (from  $\sim 1$  MHz up to  $\sim 100$  MHz) are generally more difficult to be filtered out, and they affect the performance by distorting the pulse shape of the signals, which might have a significant impact on the quality of the pulse-shape analysis process. A mesh grounding system is used for AGATA with the whole system grounded to a common voltage, which is provided by a large common conductive plate. The grounding of the mechanical structure is formed by interconnected conductive components using as short and thick grounding shunts as possible. In addition, the power distribution to the front-end components of the array is ensured via a single UPS. The measured electromagnetic compatibility performance of the AGATA front-end electronics is such that the 50 Hz noise is less than  $100 \mu\text{V RMS}$  and the high-frequency noise in the range from 0.1 MHz to 100 MHz is less than 5 mV RMS.

Table 3: Count-rate specifications and current limits in kHz after the front-end electronics, global trigger and pulse-shape analysis farm. The rates are given per crystal and for the setups with 15 and 180 crystals (AGATA  $4\pi$ ) with the nominal source-detector distance (23.5 cm).

System	Per crystal	15 crystals	180 crystals
FEE (detectors)	50 <sup>a</sup>	750	9000
Global trigger	50	750	3000 <sup>b</sup>
Pulse-shape analysis	5 <sup>c</sup>	75 <sup>c</sup>	3000 ( $M_\gamma = 1$ ) <sup>d</sup> 300 ( $M_\gamma = 30$ ) <sup>d</sup>

<sup>a</sup> With the FWHM value degraded by about 50 % compared to the nominal FWHM value obtained with a single crystal counting rate in the range 10 kHz to 20 kHz.

<sup>b</sup> Limit defined by the check idle cycles.

<sup>c</sup> Current limits of PSA processing. Writing the signal traces to disk results in a reduction of the rate to 1 kHz to 3.5 kHz per crystal.

<sup>d</sup> Full AGATA specifications rates with on-line PSA and tracking.

## 6. Front-end electronics

The objective of the AGATA front-end electronics (FEE) is to digitise the signals from each crystal, process them in real time to establish when the crystals detected a  $\gamma$  ray (marking the time with a timestamp), determine the amount of energy deposited by the interaction of the  $\gamma$  ray in each segment and extract the total  $\gamma$ -ray energy from the core contact of the crystal. The positions of the  $\gamma$ -ray interactions are calculated in the pulse-shape analysis (PSA) farm (see section 10). Therefore, the AGATA FEE supplies a short trace of the digitised leading edge of each pulse along with the energy and the timestamp. The design of the AGATA FEE has been a challenge due to the high acquisition rates specified for the system. The rate specifications and the measured values for the different subsystems are summarised in Table 3.

The PSA requires each digitizing sampling ADC to be aligned with all the others and that time-stamped data based on a common clock are generated. AGATA clock distribution and time stamping is linked to a global-trigger mechanism, which allows either free running time-stamped operation or hardware-triggered operation depending on whether data-rate reduction is needed in order not to saturate the PSA processor farm. The data sent to the PSA contain the same parameters, including timestamps, in both cases. The only difference

is whether part of the data are rejected prior to the PSA, for example because of a multiplicity condition or a requirement for coincidences with one or more ancillary detectors.

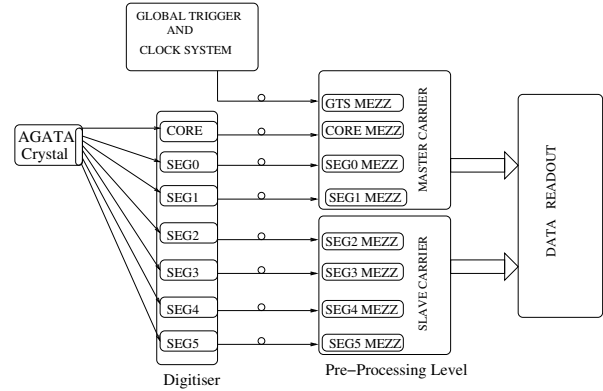


Figure 23: Schematic view of the AGATA front-end electronics and data readout system.

Fig. 23 shows the schematic design of the AGATA FEE and data-readout system, which treats each crystal (one core plus 36 segment outputs) as a separate entity. Within that entity the core is treated differently to the segments. The core signal is formed by the sum of the charge released in all the interactions in the crystal. Therefore, it can be used as a trigger for the whole crystal. The AGATA electronics for each crystal consists of the following components:

- One digitiser comprising 6 segment cards, 1 core card, 2 power-supply cards and 2 control cards.
- Two pre-processing carrier cards in the Advanced Telecommunications Computing Architecture (ATCA) card format, each containing 4 Common Mezzanine Cards (CMC) with PCI Express readout to the PSA farm. Seven CMC mezzanines correspond to the 6 segment and 1 core card in the digitiser and one contains the interface to the global trigger and clock system.

The various elements of the FEE are connected through optical fibres in order to achieve appropriate data-transmission rates and to maintain good electrical isolation.

### 6.1. The digitiser

The principal goal of the digitiser is to interface the detectors with the AGATA signal-processing system. In order to do that, the digitiser module performs the following tasks:

- Receives all 37 preamplifier outputs from one crystal.
- Digitises the input signals at a rate of 100 MHz, using 14-bit ADCs.
- Serialises the ADC data and transmits it over optical fibres to the pre-processing electronics.
- Implements a constant-fraction discriminator (CFD) algorithm in an FPGA to generate an isolated fast-logic signal to be used in hardware triggers of ancillary detectors.
- Implements a time-over-threshold (TOT) algorithm using preamplifier inhibit signals (see section 3.3).
- Provides spare digitiser channels and inspection lines for maintainability and diagnostics.
- Provides interfaces for re-programming, control in an electronics and detector workshop, as well as an interface for slow control.

The AGATA specifications require that the digitiser module is mounted less than 10 m from the detector’s preamplifiers to minimise signal degradation. The digitiser is housed in a water cooled box of the size 30 cm × 14 cm × 55 cm and it contains two modules with the electronics for two crystals. A block diagram of the digitiser is shown in Fig. 24 and a photograph of a printed circuit board for one module is shown in Fig. 25. The main building blocks of the digitiser are: the differential analogue input, the flash analogue to digital converter (FADC) sampling blocks, the field programmable gate arrays (FPGAs), which receive the FADC data and serialise it, the optical transceiver blocks, the global clock receiver block and the monitoring block. The monitoring block provides control of the spare channels and inspection lines via a slow control link to the GUI based system control software. The temperature of the various parts of the digitiser electronics is also accessible by the slow control and a local over-temperature shutdown is implemented in the control/power supply card.

The analogue input buffer adds the optional offset signal and also includes an anti-aliasing filter before the FADC. The FADCs convert the signals into 14 bits at 100 MHz; 15 data bits are sent to the FPGA for serialisation and transmission as 16-bit data over the optical fibres. Bits 0 to 13 are FADC data, bit 14 is the FADC overrange and bit 15 is used as the synchronisation pulse from the GTS (for a description of the GTS, see subsection 6.3).

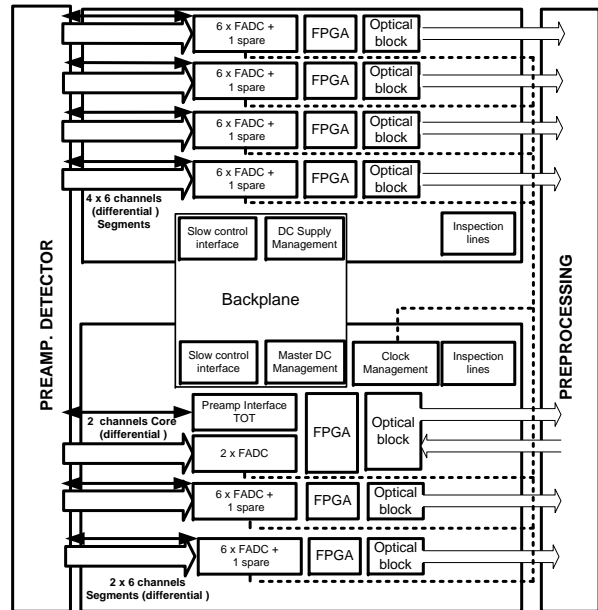


Figure 24: Block diagram of the AGATA digitiser.

Although the main purpose of the FPGAs in the segment and core cards is to serialise data, the FPGA of the core card also implements two algorithms for real-time data processing. The first is a digital CFD, which is used as a trigger for ancillary detectors (output both on an isolated connector and over a fibre). The CFD algorithm runs in the digitiser rather than in the pre-processing because of the latency of the fibre links (several 100 ns) and the need for a prompt output. The second algorithm is a TOT algorithm that measures the time during which the preamplifier inhibit signal is asserted when it receives an over-range energy input. Since the preamplifier recovers from overload by discharging a capacitor using a constant current source the period of overload (TOT) is a measure of the energy in the crystal when the preamplifier is over-range (see section 3.3). A special serial fibre protocol is used to indicate when FADC data is replaced by TOT data.

One 8 channel fibre-optic transceiver link (4 RX, 4 TX) is used to interconnect the core FADCs serialised data and the timing and control of the pre-processing subsystem. The “transmit” channels are allocated to the core 100 MHz FADC data (two channels), the core CFD logic signal (one channel), and the global clock calibration feedback path (one channel). The “receive” channels are used for the global clock signal, the synchronisation signal, and the analogue offset control for the core electronics. A 12 channel multi-fibre transmits the



Figure 25: (Colour online) Photograph of the AGATA digitiser.

6 serialised segment FADC data streams from each of the segment cards. Each analogue channel from the detector can be inspected before and after the digitisation.

One analogue line is provided before and two after coding per group of 6 segments channels. The global clock function reconstructs a high quality clock with a very small jitter ( $<7$  ps) from the clock received through one optical receiver within the core transceiver.

The digitiser is able to work in stand-alone mode when a specific firmware and GUI interface (called SAMWIZE) are used. In this mode it is possible to visualise the recorded traces from the detector input signal (oscilloscope mode). It is also possible to record up to 6 traces per segment and one per core. The Multi-Channel Analyzer mode is capable of histogramming up to 6 segment channels and one core in parallel. This mode was particularly useful for developing and testing the core energy and constant-fraction discriminator (trigger) block of the pre-processing firmware.

### 6.2. The pre-processing electronics

The pre-processing system reduces the data volume from the digitisers by a factor of about 100 by extracting and processing data from the digitiser's data stream only for the segments which have registered a detection of a  $\gamma$ -ray interaction. Further filtering (triggering) can optionally be performed in conjunction with the GTS from which a clock for the digitiser and the timestamp information is also derived. The pre-processing sends

the filtered data to the PSA farm. The processing rate for traces in the segments is the same as in the core. The triggering is always made by the core, so the core contact electronics is the master and the segments are controlled by it.

The pre-processing hardware de-serialises and processes the incoming data streams and stores the traces. The sampling speed is 100 MHz in the reconstructed data streams, so the pre-processing hardware also uses 100 MHz clock rates for incoming data (some internal clocks are running at 200 MHz). The GTS interface provides the system clock and a trigger system.

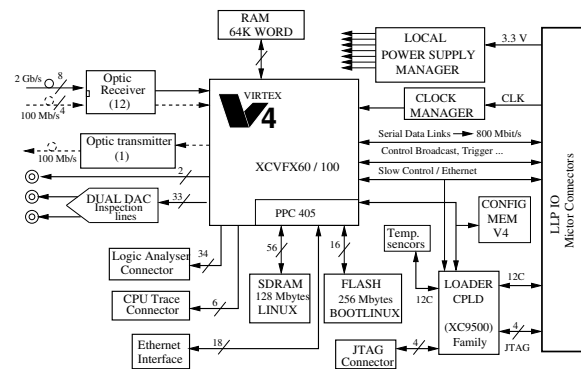


Figure 26: Block diagram of the AGATA pre-processing mezzanines.

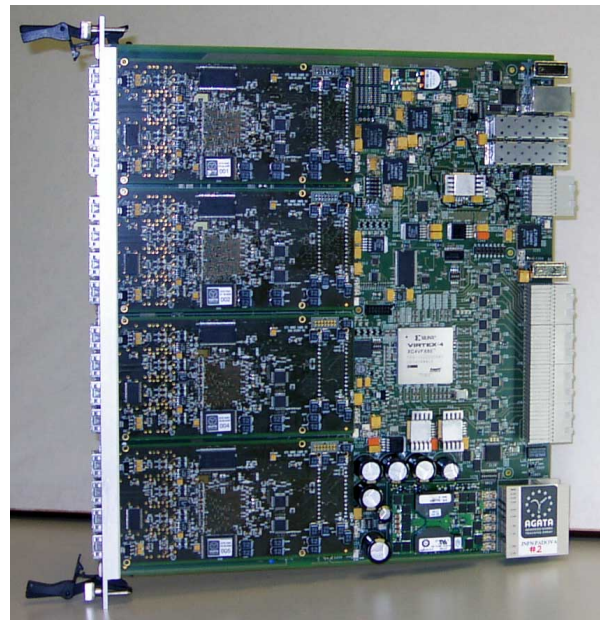


Figure 27: (Colour online) Photograph of the AGATA pre-processing ATCA carrier card.

The AGATA trigger system can be used to reduce the

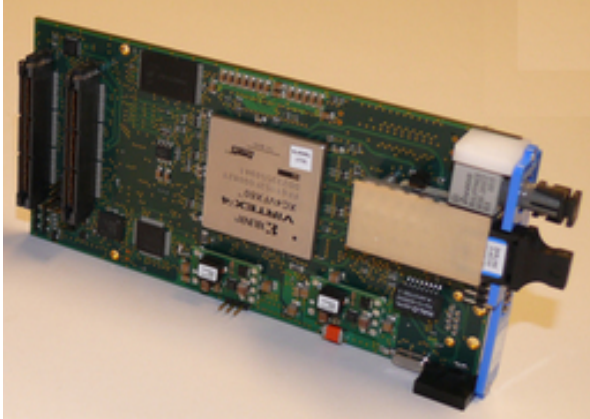


Figure 28: (Colour online) Photograph of the AGATA pre-processing mezzanine card.

counting rate. Where rate reduction (see Table 3) is not required, the pre-processing runs in triggerless mode, which means that all the processed data are sent to the PSA farm. In this case a software trigger is performed after PSA and tracking. The maximum delay (latency) which can be accommodated in the pre-processing hardware while waiting for a trigger decision is limited by the maximum of the trace length, which is  $20\ \mu\text{s}$ . Lower values can be configured in the trigger system, but coincidences separated by more than  $20\ \mu\text{s}$  are detected by using software triggers.

The local trigger of the core signal is a digital-trigger algorithm operating on the data stream from the core contact of the crystal. When this trigger finds a pulse in the data it generates a local trigger output which indicates to all the segment electronics that they should also extract a trace from the data stream. Traces are stored locally, within each pre-processing channel. The traces are held in each channel's local memory for up to  $20\ \mu\text{s}$  while the GTS makes a decision. An event can be either accepted or rejected. For events which are accepted, the pre-processing stores a trace of the digitised leading edge of the pulses from the core and from all 36 segments in a buffer waiting to be sent to the PSA farm.

In addition to selecting useful portions of the incoming data stream using a trigger algorithm, the pre-processing also applies the moving window deconvolution (MWD) algorithm [39, 40] on the incoming data streams to determine the  $\gamma$ -ray energy deposited in each segment and in the whole crystal. The MWD filter output is sampled a programmable time after the trigger algorithm detects the start of a digitised pulse in the incoming core data stream. The energy parameter sampled from the MWD filter is stored along with a data trace showing the samples taken during the leading edge

of the pulse and a timestamp indicating when the trigger happened.

Core and segment mezzanines have PowerPC processors with an embedded Linux operating system housing all the drivers and applications for the card control and online temperature monitoring. A slow control GUI, based on a web server architecture, has been developed for the control and online monitoring of the status of the mezzanine cards. The block diagram of the pre-processing mezzanine is shown in Fig. 26. Photographs of the printed circuit boards of the carrier and mezzanine cards are shown in Fig. 27 and 28, respectively. Carrier cards, implemented in the ATCA standard [41], house the CMC format mezzanines, which read data from the core and segment cards in the digitiser and a GTS mezzanine, which communicates with the GTS system.

A block diagram of the GTS mezzanine is shown in Fig. 29 and a photograph of the printed circuit board in Fig. 30. The GTS mezzanine receives the global clock, aligns it locally within the pre-processing and then uses a dedicated data path in the core mezzanine to align the clock in the digitiser. It is also used to accept or reject local triggers. The core and segment mezzanines receive data from the digitiser and process the data using digital filter algorithms. The mezzanines are read out via the carrier, all data being concentrated into a single FPGA per carrier before transmission via PCI express to the PSA farm on demand by the PSA. The carrier reads each mezzanine at 100 MB/s. A different FPGA handles the trigger interconnections within the carrier. Trigger connections between the two carriers handling one crystal use a dedicated backplane link (TCLK). The ATCA carrier cards accept 4 CMC format mezzanines. The connection between the CMC and the carrier card is achieved by two Mictor connectors, each with 114 pins.

### 6.3. The Global trigger and synchronisation (GTS) system

Data synchronisation is an important aspect in the operation of the trigger and readout systems of AGATA. Tracking and PSA require the concurrent digitisation of preamplifier signals of the 36 segmented Ge crystals composing the array. Therefore, the design of the front-end readout and level-1 (L1) trigger in AGATA follows a synchronous pipeline model: the detector data are stored in pipeline buffers at the global AGATA frequency, awaiting the global L1 decision. The L1 latency must be constant and match the pipeline buffer length. The whole system behaves synchronously and synchronisation at different levels and in different contexts has

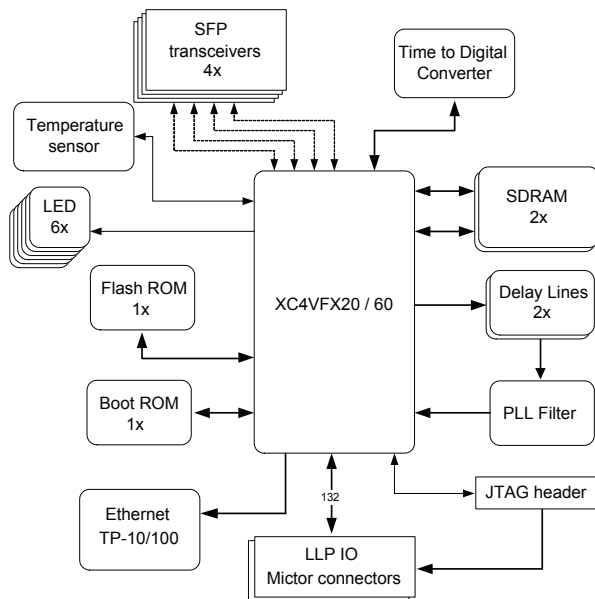


Figure 29: Block diagram of the GTS mezzanine.

to be achieved and monitored for proper operation of the system.

In AGATA each crystal is considered as a separate entity and, from the point of view of the data acquisition system, the whole detector may be considered as the aggregation of synchronised data supplied by individual crystals, possibly disciplined by a global trigger primitive.

The data from the core contact are processed for event detection and either an L1 trigger request or a local trigger is generated. The choice between the two behaviours is done upon configuration, the former corresponding to an effective way to reduce front-end data rates in cases where any one of the stages of the readout chain is unable to perform at the actual data throughput. From the logical description of the front-end operation given above it turns out that a certain number of global time-referenced signals are needed. The most important of these are: the common clock, the global clock counter, the global event counter, the trigger controls, the trigger requests and the error reports. In AGATA, the transport medium of all these signals is shared by use of serial optical bi-directional links connecting the FEE of each crystal with a central global trigger and synchronisation control unit in a tree-like structure; thus actually merging together the three basic functionalities of synchronisation distribution, global control and trigger processing.

The common clock is a 100 MHz digital clock sup-

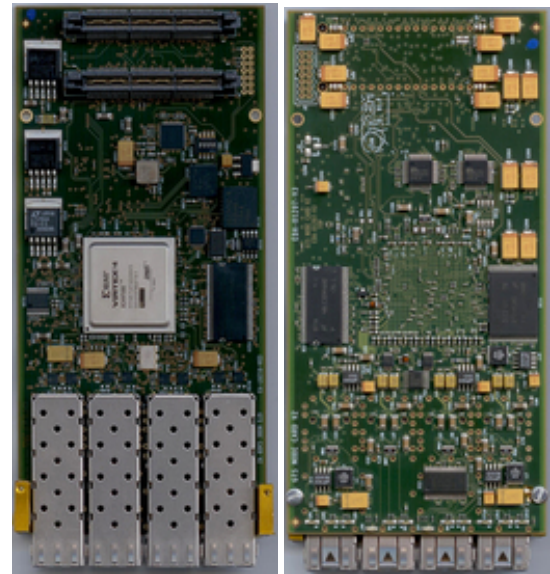


Figure 30: (Colour online) Photographs of the two sides of the GTS mezzanine.

plied by a central timing unit and used to clock the high-speed optical transceivers reaching the FEE of every crystal. At the crystal receiving side the clock is reconstructed and filtered for jitter. The clock signals of each crystal may be equalised for delay and phase; thus accounting for different fibre lengths and different crystal locations in the array.

The global clock counter is a 48-bit digital pattern used to tag event fragments before front-end buffer formatting. The pattern is the actual count of the global clock. It will be used by the PSA processing and by the global event builders to merge the event fragments into one single event. The global event counter is a 24-bit digital pattern used to tag event fragments before front-end buffer formatting. The pattern is the actual count of the L1 validations. The trigger control must guarantee that subsystems are ready to receive every L1 accept delivered. This is essential in order to prevent buffer overflows and/or missed trigger signals when the crystals are not ready to receive them. In either case, the consequence would be a loss of synchronisation between event fragments.

The trigger requests are generated by the core contact signal from the AGATA detectors by asserting a signal that is transmitted via the high-speed serial links of the GTS network upwards to the central trigger unit. All the trigger requests collected from the crystals at each global clock cycle form a pattern that can be processed centrally for multiplicity or coincidence with ancillary detectors. The result of this processing stage consti-

tutes the L1 validation. Error reports indicate abnormal conditions such as buffer overflows, local faults, built-in self tests, etc., and can be reported centrally for proper corrective actions.

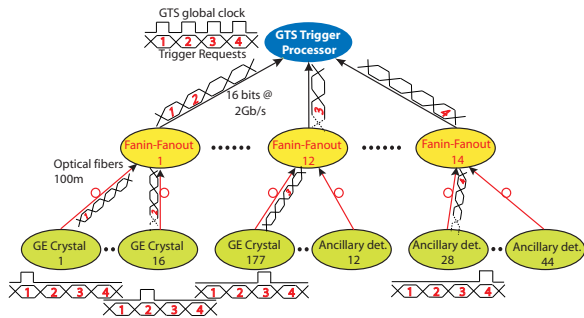


Figure 31: (Colour online) Illustration of the topology of the GTS tree. Any detector node can produce at any time a trigger request, which is labeled with the clock and transmitted upwards in the tree, through the fan-in-fan-out architecture to the global trigger processor.

The AGATA GTS has a tree topology as shown in Fig. 31. The tree originates from the root node, which at the same time acts as the source of all global information (clock, timestamps, commands, L1 validations) and all the trigger requests. It also performs fast monitoring of signals and services requests coming from the crystals. To solve the problems of building a bi-directional, high-capacity and high-speed network tree that drives hundreds of nodes which are displaced by several tens of meters, a certain number of technological issues have been addressed. Among these issues are the fan-out of a source synchronous transmission, noise immunity, low error rate and throughput. The GTS tree is composed of five different elements: the root node, the backplane, the fan-in-fan-out nodes, the fibre connections and the mezzanine interface.

At the root node, a fast optical link forwards all the collected trigger requests to the trigger processor, which is a high-performance and fully-pipelined custom-built processor that sorts incoming requests, computes multiplicities and prompt or delayed coincidences among seven user defined trigger partitions. The trigger processor is fully programmable in the C programming language by the user through an application programming interface and it is controllable via a standard PCI express interface.

## 7. Coupling of complementary instrumentation

The coupling of large  $\gamma$ -ray detector arrays, such as EUROBALL [4] and GAMMASPHERE [5], to complementary detectors has played a major role in spectroscopic investigations in the last decade. The AGATA array will be used with radioactive or high-intensity stable beams and in most experimental conditions, in order to fully exploit its capabilities, it will be essential to couple it to devices providing complementary information. Additionally, the foreseen use of AGATA at different facilities makes some of the complementary devices (e.g. beam-tracking devices in the case of fragmentation facilities) absolutely necessary for the normal operation of the array.

Within the AGATA project, dedicated new complementary detection systems will be developed in addition to adapting existing ones. The use of fully digital sampling electronics is desirable in the future. However, in order to utilise the many existing systems based on conventional analogue readout electronics an interface to the GTS system has been developed. This interface is called AGAVA (AGATA VME Adapter). Since nearly all of the presently available detectors within the AGATA community have front-end/readout systems based on the VME or VXI standard, the AGAVA interface has been developed in the VME standard with full compatibility with the VXI readout modes.

### 7.1. General description of AGAVA

The AGAVA Interface is a one-unit wide A32/D32 type VME/VXI slave module. It is the carrier board for the GTS mezzanine card used in AGATA for the global trigger and timestamp distribution.

The main purpose of the AGAVA interface is to merge the AGATA timestamp-based system with conventional readout based on VME or VXI, which is used for example by EXOGAM [42]. AGAVA also has the necessary connectors to interface with the VME Metronome and SHARC [43] link systems. The logic process is controlled by an FPGA of the type Virtex II Pro. The block diagram of the AGAVA interface is shown in Fig. 32. The AGAVA module (see Fig. 33) includes all necessary connections for the trigger cycle and for a total data readout system [43]. It contains also a passive Ethernet interface, which provides a direct connection to the GTS mezzanine card.

### 7.2. The operation of AGAVA

The AGAVA module supports VME access, provides interfacing with the GTS mezzanine and provides input/output signals at the front-panel Lemo connectors.



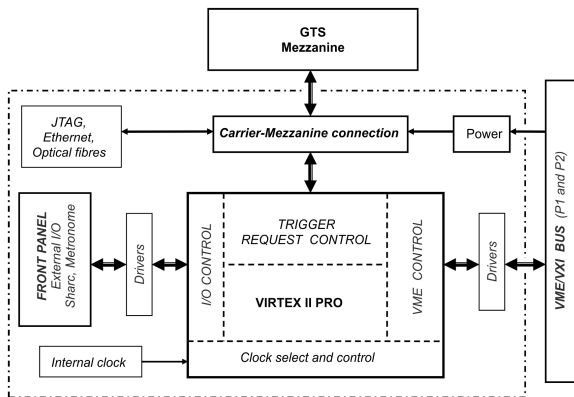


Figure 32: Block diagram of the AGAVA interface.

Two VME access modes have been implemented in AGAVA: the VME single-access read or write operations, according to the standard VME handshake rules, and the chained block transfer (CBLT) readout mode on the VME bus. Standard access can be used both for board configuration and readout, while the CBLT mode (available in many commercial VME ADC and TDC front-end modules) has been introduced to speed up data readout. The CBLT mode makes use of a common address specified during the initialisation phase in a dedicated register for all participating modules in the chain. The VME CPU reads their data in blocks of variable lengths starting from the module defined as the first in the chain, followed by one or more intermediate modules and finished by the one configured as the last one. The CBLT mode is used for faster readout and is helpful for event building. The CBLT readout mode of AGAVA has been extensively tested. The AGAVA interface also implements a VXI EXOGAM-like readout.

The interface to the GTS mezzanine provides the full trigger-request/validation/rejection cycle and acquires also the clock tag and the event number, the latter only in case of a validated cycle.

The AGAVA module receives, through the front-panel input, the trigger requests from the complementary detector (named here *external* trigger) that is passed as a single 10 ns wide pulse to the GTS system (an *internal* trigger request can be generated for testing purposes). After the trigger request is passed to the GTS system, the AGAVA module receives the local trigger signal and tag and waits for the validation or rejection signal and tag coming from the GTS System. The latency time to receive the validation or rejection depends on the GTS tree architecture and is of the order of 12  $\mu$ s.



Figure 33: (Colour online) Photograph of the AGAVA module with the GTS mezzanine card.

Information is stored in registers or RAM memory (depending on the firmware functionality mode). Once the information is stored, the AGAVA module sets the data ready flag to inform the VME or VXI system that the data can be readout by the CPU module and transferred to the event builder. The busy flag is set after accepting every trigger request. The release of the busy (i.e. ending the dead time for new triggers) strongly depends on the VME/VXI readout mode and speed. In case of high trigger rates, the backpressure front-panel input can be used to reduce the trigger request to the GTS system.

In order to support the wide range of complementary instruments, two different AGAVA functionalities have been introduced: common dead-time mode and parallel-like mode.

In the common dead-time mode only one trigger at a time is accepted. The trigger request, acknowledged only if the AGAVA module is not in busy status from the previous cycle, sets the busy state until all data are readout by the CPU module.

In the parallel-like mode, when a trigger request arrives on the front-panel input, the AGAVA module sets

and holds its busy status only until the local trigger and local trigger tag are received from the GTS mezzanine card and are stored in the AGAVA multi-event RAM. A new trigger request can be accepted afterwards by the AGAVA module avoiding the GTS latency time and with a sizable reduction of the total system dead time. The flow of validation or rejection triggers and tags received by the AGAVA module are compared with the local ones present in the multi-event RAM and if they match correctly the VME/VXI CPU can read the relative data.

## 8. Data acquisition

As shown in Fig. 34, the data acquisition (DAQ) system receives the preamplifier traces from the FEE and processes them into several stages up to the storage of reconstructed events; see section 8.1 for a description of the data flow. Services described in section 8.2 are needed to control and monitor the whole system including the electronics. For a complex instrument such as AGATA, large computing, network and storage capabilities are needed, as will be discussed in section 8.3.

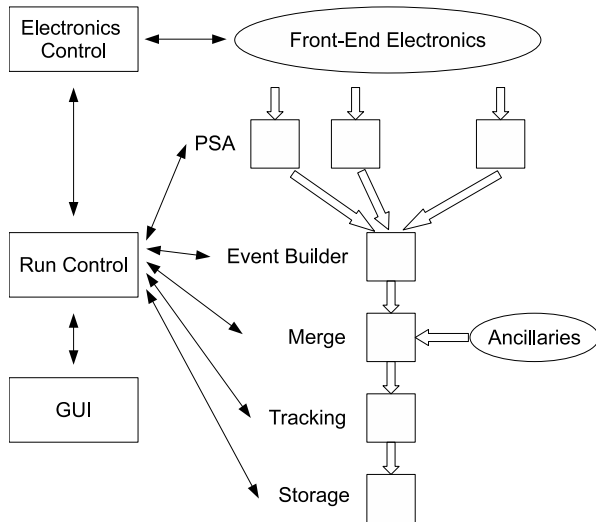


Figure 34: Layout of the AGATA data acquisition system.

### 8.1. Data flow

The data flow integrates the algorithms needed to process the information from the interaction points. At the end of the chain, data have to be provided to the users in the AGATA Data Flow (ADF) library [44]. After the PSA, data from all crystals are merged together taking into account the physics correlations provided by

the pre-processing electronics. These correlations can be based on timestamp or event number depending on which AGATA trigger mode is used (see section 6) If additional detectors are coupled to the AGATA array, the corresponding data flow is assembled in the same way. After this procedure tracking is performed to reconstruct the  $\gamma$ -ray trajectories. This procedure is then followed by the data storage on a large local disk array before being sent to Grid Tier1 computing centres based at INFN-CNAF in Bologna (Italy) and at CC-IN2P3 in Lyon (France). It is also possible to write data to disk at each step of the data flow.

Because of the high rate specifications (50 kHz per crystal, see Table 3) and the required processing power and large data transfer bandwidths, the algorithms have to be distributed over several computers (CPUs and cores) At this high rate the storage of 200 B per segment and core gives a data rate of about 400 MB/s per crystal at the output of the FEE. The data flow and embedded algorithms are managed by the Narval [45, 46] framework. Narval is a highly-distributed data acquisition system running across a network and acting like a single program that transports the data to the storage of the reconstructed events. Narval is based on actors corresponding to separate processes that receive and send out data at any stage of the data-flow chain. It is developed in Ada for a high reliability and safety level and it is very flexible since the actors can load C and C++ shared libraries.

The event-builder and merge algorithms are written in Ada while the PSA and tracking algorithms are written in C++. The originality of the DAQ system relies on the development of the ADF framework [44], which has been designed in order to facilitate the separation between data transport and algorithm development. ADF provides the interface between Narval and the algorithms (PSA and tracking). It also allows to encode/decode the data at various stages of the data flow. ADF can be either used with Narval or as a stand-alone library for data replay and it is part of the GammaWare package [47] (see section 12).

In order to survey the data acquisition system, Narval provides a “spy” mechanism by which it is possible to sample pieces of the data flow from each actor for control, monitoring and online analysis purposes. The spy is available to any client connected to the DAQ services network.

### 8.2. Services

A set of services are provided to control and monitor the whole system including the detector electronics. The run control centralises information from different

subsystems of AGATA. It also collects messages, errors, and provides an ELOG logbook [48] for the users. A GUI is provided for the electronics and run controls.

#### 8.2.1. Run control

The main purpose of the run control (RC) is to control and monitor the DAQ components. It coordinates the large number of activities that are necessary to achieve an operational state for the AGATA detector including the DAQ system. Actions like initialisation, setup of several components, start and stop of the data acquisition, are performed by the operator through the RC system. The RC interacts with the electronics control system, which is in charge of the control of the hardware devices. The RC also provides the monitoring of the data acquisition (input rate, buffer occupancy, error rate, etc.), error report, error handling functionalities and logging capabilities. The RC is based on the middleware produced by GridCC [49]. To communicate with all the controlled components a standard WSDL (Web Services Description Language) interface has been defined.

#### 8.2.2. The Cracow graphical user interface

The GUI known as “Cracow” [50] allows the user to perform commands such as loading the configuration, starting and stopping the DAQ system, etc. All the possible states of the DAQ state machine are reflected in the GUI by a set of buttons that allow particular actions to be performed. Cracow is an independent tool, which communicates with the RC through the web services. It can be run on any computer connected to the AGATA network. As mentioned before, Narval is a system whose actors (algorithms) are highly distributed, which means that the user can create actors on many different processors. A configuration of these actors is called a topology. The Cracow GUI can show a working diagram of the currently loaded topology. The graph is constructed based on information delivered online by the actors. They send information about themselves and about their direct collaborators.

#### 8.2.3. Spectrum server and viewer

The different algorithms implemented in the DAQ provide spectra or matrices. In order to collect histograms from the various sources, the GRU spectrum server (GANIL Root Utilities) [51] has been implemented. As soon as a root histogram is added in the GRU database, it is immediately available on the network and can be displayed by any client like ViGRU [51] or the “Cracow” GUI described above.

#### 8.2.4. Electronics control

The electronics control (EC) system is an ensemble of software tools that allows to setup of all the electronics subsystems (digitisers, pre-processing, GTS and possibly ancillary electronics) and to monitor some key parameters. The main functionalities to be provided by the EC system are the following: the description of the system insuring its coherency, the localisation of the servers controlling each subsystem, the initialisation of the different devices with the correct values, the saving of all the setup parameters for the whole electronics or a part if necessary, the restoration of a previously saved setup, the monitoring of key parameters in the different boards, the handling of error/alarm events passing them to the RC. The EC system has to insure the integrity of the system and the synchronisation of the state machine of the different subsystems. It accepts a set of simple commands from the RC (setup, go, stop, get state, etc.).

The EC system is designed with a client/server approach and with partitions accordingly to each type of hardware. There is one EC subsystem with its engineer-oriented GUI for each type of hardware, i.e. one EC subsystem for digitisers, one for carrier boards, one for core/segment mezzanines, one for GTS and one for ancillary electronics. In order to centralise the different electronics subsystems, a Global Electronics Control (GEC) based on the ENX [52] framework has been designed. The GEC acts as a coordinator between the different subsystems and the RC.

#### 8.3. Hardware implementation

The system first implemented for AGATA at LNL has been designed to be scalable to cope with the full array specifications, easily movable between different host sites and easily maintained by the collaboration. The AGATA DAQ hardware (servers, disk, local network, etc.) and software should be seen from the host laboratory as a black box.

On the hardware side, there is a big requirement for computing power to run algorithms hosted by the data acquisition (PSA, event-builder, merge, tracking). Each crystal is attached to one PSA server. Since the PSA processing is the most demanding part of the system, Narval distributes events on the different cores of each PSA server. There is also one server for event building, one for merging with ancillary devices, one for tracking, three disk servers, two for slow control, two for DAQ box control, and two for data analysis. All servers are identical and connected to a KVM (Keyboard Video Mouse) switch to ease the hardware maintenance. The model chosen is the IBM® x3550 1U server (from initial to M3 versions) with 2 quad cores Intel® Xeon®

CPUs each, which allows the PSA algorithms to be run at a crystal rate of about 4 kHz. The Debian distribution [53] of the GNU/Linux operating system is installed on all machines.

AGATA generates a large data flow, which must be stored at very high rate, especially when traces are stored. The local disk array of AGATA consists of 4 disk servers. Three of them are attached to a SUN® Storage Tek™ 6540 fibre channel system with 112 TB of disk (90 TB using RAID 6) and shares data using the GPFS (General Parallel File System) clustered file system. A fourth server attached to the storage system provides the interface to the Grid for further data storage or analysis (see section 12). Many services are needed to handle the DAQ box: monitoring, documentation (Wiki documentation mirrored on the main DAQ web site [54]), network control, installation server, hardware monitoring using Zabbix [55], etc. These services are hosted on a virtual Xen [56] machine. A backup system is installed on a SUN® Fire™ X4560 system with 8 TB of disks to save periodically the vital elements of the DAQ box.

In order to reduce the dependency particular to the host laboratories, basic network services are provided in the DAQ box: DHCP (Dynamic Host Configuration Protocol), DNS (Domain Name System), software distribution, etc. External users (developers, system administrators) can access the DAQ box through a VPN (Virtual Private Network).

Networking is an important issue having in mind the high data rates foreseen in forthcoming AGATA experimental campaigns. The communication between nodes is organised around two different networks, one for data acquisition called DAQ network and the other for network services called DAQ services.

The data acquisition infrastructure can be hosted in one or several buildings. For example at LNL, the Tandem accelerator building hosts the data flow and DAQ services machines while the Tier 2 computer room hosts all the disk servers. Both rooms are connected with 3 GB optical links.

### 8.3.1. Algorithm for compression of traces

In order to reduce the size of the stored traces a simple algorithm has been devised to compress the traces to about one half of their original size. The compression algorithm is based on the observation that the difference between the measured voltages of two consecutive sampling points is small. Fig. 35 shows a typical spectrum of differences between neighboring sampling points. The spectrum is broad with a very sharp peak

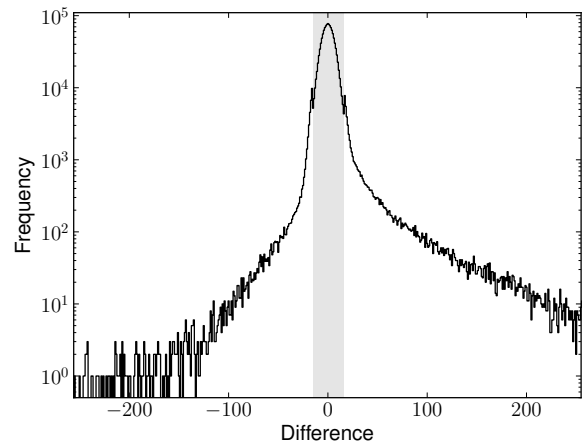


Figure 35: (Colour online) Typical difference spectrum of recorded traces. The parameter on the horizontal axis is the difference in the value of two consecutive sampling points. The shaded region, which marks difference values from  $-31$  to  $+32$ , contains 93 % of the data. The histogram contains data from about 13 million sampling points.

around zero difference. The mean value of the distribution is positive because the traces are recorded at the beginning of the pulse to cover the leading edge of the signal.

The sampling points have a 14-bit resolution and are stored by the pre-processing electronics in 16-bit unsigned integer values. The trace length is typically 100 points. In Fig. 35 one may see that about 93 % of the difference spectrum is contained in the region between  $-31$  and  $+32$ . This fact will be used for the compression as several of these small differences can be packed into 16 bits. The chosen storage format is the following:

- The first sampling point of the trace is always stored with its original value. It becomes the first reference point.
- If three consecutive sampling points after the reference point differ from their respective previous sampling point by values between  $-15$  and  $+16$ , the three differences are encoded in  $3 \times 5$  bits in a 16-bit unsigned integer with the most significant bit set to 0.
- If one sampling point after the reference point differs from the reference by a value between  $-31$  and  $+32$ , the difference is encoded in an 8-bit unsigned integer with the two most significant bits set to the binary value 10.
- Otherwise, the 14-bit value is stored in a 16-bit unsigned integer with the two most significant bits set to the binary value 11.

- Finally the reference point is advanced to the last point stored so far.

For most of the sampling points of a trace, three consecutive points from originally three 16-bit words can be packed into a single 16-bit word. For traces with 100 points excluding the headers of the data, a compression of about 38 % is achieved. The compression of data containing both sampling points and data headers is typically about 44 %.

## 9. Pulse-shape simulations

In order to realise the real-time localisation of the scattering sequence following a  $\gamma$ -ray interaction inside an AGATA detector, the experimentally digitised pulse shapes will be compared with a basis data set. For on-line pulse shape analysis (PSA) to be implemented successfully, it has been estimated that more than 30 000 basis sites per crystal for a 2 mm Cartesian grid [57] are required. The basis can be obtained from either experimental or simulated data. However, presently the time prohibitive nature of the experimental methodology (see section 4), means that the only practical way to generate a full basis is by calculation.

The AGATA collaboration has therefore developed electric field simulation codes such as Multi Geometry Simulation (MGS) package [58], the Java AGATA Signal Simulation (JASS) toolkit [59] and the IKP Detector Simulation and Optimisation method now called the AGATA Data Library (ADL) [60–63], in order to facilitate the realisation of the on-line PSA. These codes have been used to generate variants of a single crystal basis and an earlier code originally developed for the MARS project [11] was used to optimise the physical segmentation scheme in the depth of the AGATA crystal.

In general, the electric field simulation codes use finite-element methods for solving partial differential equations, such as the solution to Poisson’s equation. Environments such as FEMLAB and DIFFPACK can also be adapted for providing an analytical solution to the complex electric field distribution inside the AGATA crystals. The codes utilise the approach shown in block format in Fig. 36. The calculations are performed on a user specified 3D grid that maps a given detector volume. Results from each stage of the calculations are stored in matrices. The values at each point in the matrices are then recalled to generate the pulse shape response, as determined by the trajectories of the charge carriers through the weighting field [64].

The MGS package [58] utilises MatLab’s matrix environment to derive the expected pulse-shape response

at the contacts of any geometry of HPGe detector. The stand-alone package has been compiled for use with both Linux and Microsoft Windows operating systems. MGS was developed as an alternative specialised solution to the commercial packages.

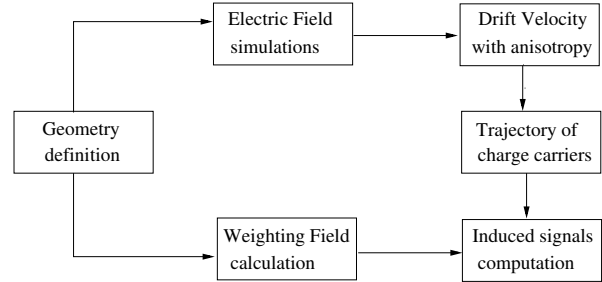


Figure 36: Data flow diagram for the simulation of the expected pulse shapes at the contacts of any arbitrary HPGe detector geometry. For a given detector, the crystal volume can be divided into a cubic matrix of lattice sites. Values for the electric potential, electric field and weighting field are calculated at each position. The drift velocity matrices are calculated from the electric field matrix. The detector response for a given interaction site is calculated by tracking the trajectory of the charge carriers through the weighting field [64].

The top panel of Fig. 37 shows the geometry of the AGATA symmetric prototype crystal as generated by MGS. The middle panel shows the electric potential and the bottom panel the electric field values in the  $z$ - $x$  plane at  $y = 51$  mm (centre of the crystal). The results show the decrease in potential and field strength as a function of increasing radius from the central anode. The figure clearly illustrates the complex nature of the electric field within the closed-end coaxial geometry of the AGATA crystal.

At high electric fields and low temperatures the charge carrier drift velocities in germanium become anisotropic [65]. They depend on the electric field vector with respect to the crystallographic lattice orientation. The electron drift velocities,  $v_e$ , are saturated at field strengths  $>3000$  V cm<sup>-1</sup> for the  $\langle 100 \rangle$  and  $\langle 110 \rangle$  directions, and at  $\sim 4000$  V cm<sup>-1</sup> for the  $\langle 111 \rangle$  direction. The hole drift velocities  $v_h$  are saturated for fields  $\sim 4000$  V cm<sup>-1</sup> along all three major crystallographic axes. The models for anisotropic drift of the electrons and holes in  $n$ -type HPGe detectors implemented in MGS have been derived from work published in [60] and [66], respectively.

Before the induced current at each electrode can be calculated, the weighting potentials and weighting fields must be generated. The calculation is performed with a null space charge density and with +1 V on the sensing electrode with all other electrodes grounded. For

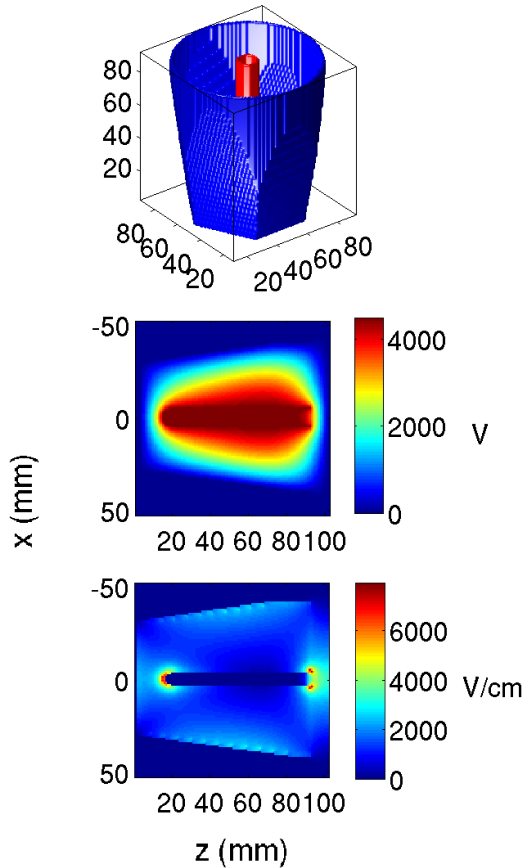


Figure 37: (Colour online) An MGS simulation of the AGATA symmetric prototype crystal geometry (top). Electric potential (middle) and electric field values (bottom) in the  $z$ - $x$  plane at  $y = 51$  mm (centre of the crystal). The results show the decrease in potential and field strength as a function of increasing radius from the central anode.

a given interaction position, the charge-pulse response observed at any electrode depends on the trajectory of the charge carriers through the weighting potential of that electrode.

The experimental characterisation data sets have been used to adjust and optimise the parameters of the code. Fig. 38 shows an example comparison between the average experimental pulses collected from AGATA crystal C001 and the ones calculated with MGS.

The JASS toolkit [59] provides a Java-based pulse-shape simulation using a very similar logic structure as MGS shown in Fig. 36. In addition, it allows for a much higher granularity in the grid as well as a more precise description of the complex geometry of the AGATA detectors and the processes at the segment boundaries. In connection with an extremely accurate interpolation method the description is very precise, especially in the

critical regions of the crystals. With its automated generation of the signal basis for the AGATA detectors an excellent agreement between simulated signals and the experimentally characterised detector signals has been found.

The ADL package [60–63] allows for the simulation of the position-dependent detector response to  $\gamma$ -ray interactions. This library was written in C and it is used to create a pre-calculated set of position-sensitive detector responses. Such sets are used as a lookup table to translate online acquired signals into position information. ADL makes use of realistic anisotropic electron and hole-mobility models specially developed for germanium. The code has a unique capability to simulate partially depleted detectors and their capacitances and this feature allows for the space-charge reconstruction in highly-segmented detectors from capacitance-voltage measurements [67, 68]. The code was recently also successfully used to simulate the position-dependent collection efficiency within the AGATA detectors. Such efficiencies can be used to correct for trapping effects by exploiting the high position sensitivity of the detectors [69]. The approach utilises the radial dependence of the trapping magnitude which allows a parametric correction to be applied.

A code based on the chain of free open-source software OpenCASCADE [70], gmesh [71], libmesh [72], and GSL [73], called AGATAGeFEM [74] has also been developed. The open-source software are used to model the geometry, to create a mesh adapted as a function of the field shape for the solving of the partial differential equations, to solve these equations, and finally to solve the problem of transporting the charges inside the crystal and the formation of the signals. The response of the preamplifier and crosstalk are included. A pulse-shape database calculated using this code has yet to be tested with real data.

## 10. Pulse-shape analysis

The task of pulse-shape analysis (PSA) is to identify with high precision the location of the individual interaction points and the corresponding energy deposits of a  $\gamma$  ray. A  $\gamma$  ray will normally have a chain of interactions in the shell of germanium detectors (e.g. 3 to 4 at 1.3 MeV). There can be more than one interaction in one detector segment and/or the  $\gamma$  ray can be scattered to another segment of the same crystal or to an adjacent detector, or even across the shell. The accuracy of the location of these interaction points has to be better than 5 mm (FWHM). Such a high precision is required in order to perform the tracking process with high efficiency.

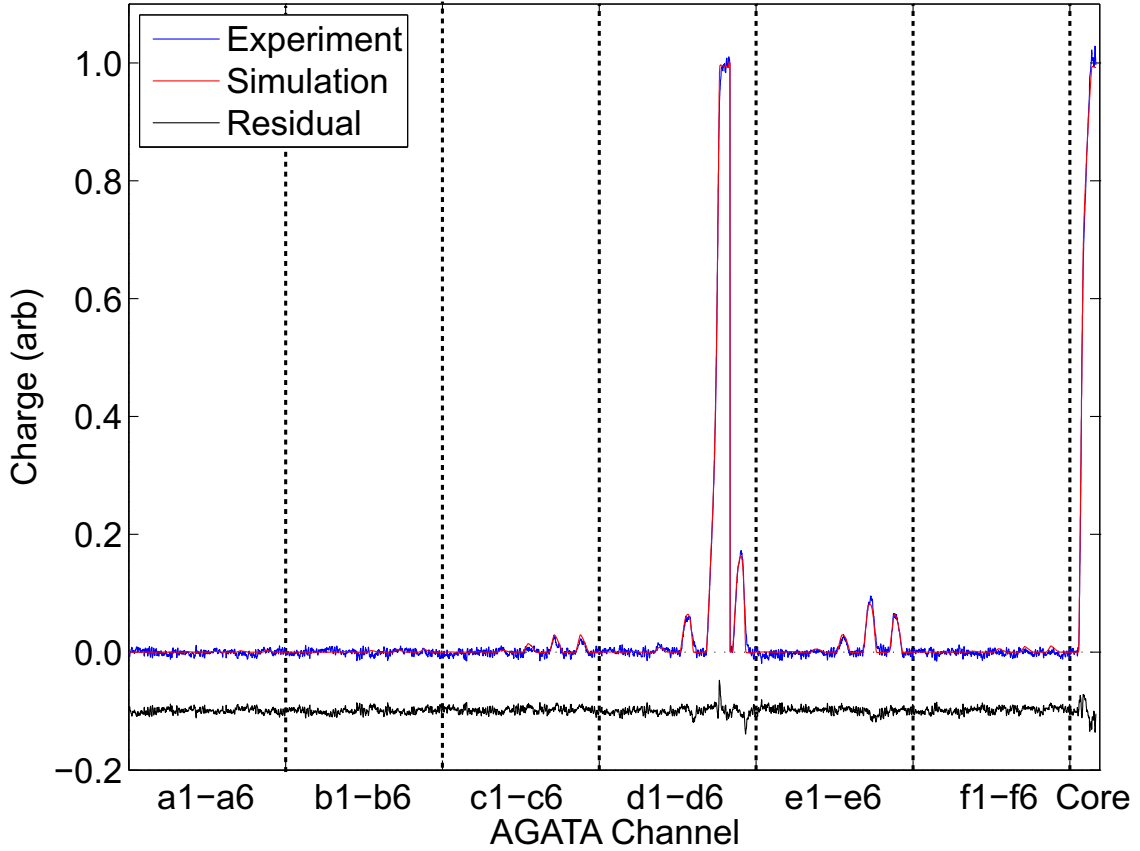


Figure 38: (Colour online) A figure showing the 37 charge pulses from the C001 detector for an interaction in a "true coaxial" region of the crystal in segment d5. The average experimental pulses are shown in red, the MGS calculated responses are shown in blue and the difference in magnitude between the two pulse-shape data sets is shown in black. The difference is shifted down by 0.1 for clarity. These data were obtained from a coincidence scan using a  $^{137}\text{Cs}$  source of 662 keV  $\gamma$  rays. The AGATA detector records the 374 keV  $\gamma$  rays that have been Compton scattered by  $90^\circ$ .

The location and energy determination must be performed by algorithms that are fast enough for real time application, with the computing power available. Indeed, the high experimental event rate multiplied by the data rate of the digitiser produces an information flux far beyond the realistic disk storage capacities in terms of volume and recording speed rate. Data from a set of  $37 \times 100$  ADC samples delivered by the digitiser are reduced through PSA to few parameters of interest. These are determined, by comparing the detected pulse shapes to a calculated reference basis, in real time. This provides the three dimensional interaction position, energy, time and a confidence in the quality of the determined fit.

A set of algorithms, such as grid search [57, 75], genetic algorithms [76], wavelet decomposition, and a matrix method [77, 78], optimised for different types of

events, have been developed. A first operational version of the PSA code, a stepwise refined grid-search [57], has already been implemented in the final Narval environment. Other faster algorithms, which have been extensively tested with simulated data and are suited to more complex event structures, will be implemented in the near future. It is expected that the performance of PSA will continuously improve during the project due to refined algorithms and increased computing power but especially due to improvements in the quality of the reference signals.

The approach based on a genetic algorithm aiming for a full decomposition was found to be too slow for online processing [76]. Therefore, the collaboration focused initially on the grid-search algorithm [57], which due to its simplicity is the most robust among the signal decomposition codes.

The code based on the grid-search algorithm has been validated with experimental data obtained in two in-beam experiments using techniques based on Doppler effects of  $\gamma$  rays emitted by nuclei in flight [79, 80]. The first experiment was performed at IKP Cologne with the prototype ATC detector, which consisted of three symmetric HPGe crystals [79]. The second experiment was the first in-beam AGATA commissioning experiment performed at LNL with the first production series ATC detector, which consisted of three asymmetric HPGe crystals [80]. The measured interaction position resolution versus  $\gamma$ -ray energy obtained in the latter experiment is shown in Fig. 39. The grid-search algorithm has also been validated in a measurement with the setup at LNL using a  $^{22}\text{Na}$  source [81].

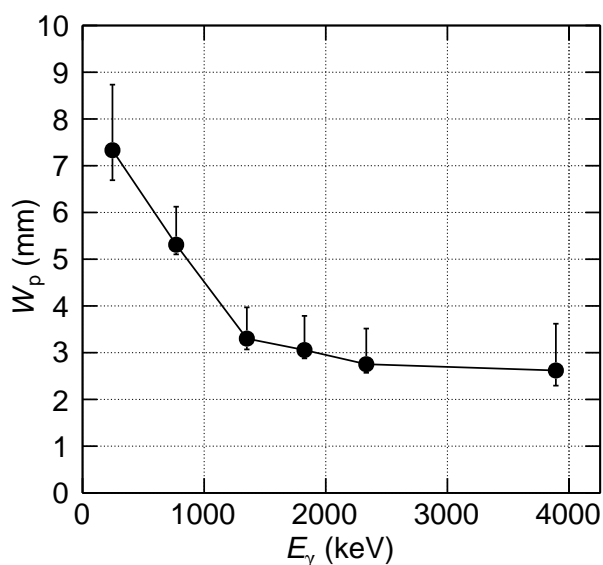


Figure 39: Interaction position resolution  $W_p$  (FWHM) versus  $\gamma$ -ray energy  $E_\gamma$  extracted from the data obtained in the first AGATA in-beam commissioning experiment based on an inverse kinematics fusion-evaporation reaction with a 64 MeV  $^{30}\text{Si}$  beam and a thin  $^{12}\text{C}$  target. The error bars include both statistical and systematic errors. See [80] for further details.

It was shown that in the case of single-hit events the grid-search algorithm already gives a sufficiently good Doppler correction. However, it is not well suited to more complex events, the reason being that in the case of multiple interactions in a crystal, or especially in a segment, the analysis effort strongly increases with the number of degrees of freedom. However, the grid-search algorithm has been used successfully with in-beam data to handle multiple interactions in the same crystal as along as the segments with transient signal do not overlap.

Several fitting procedures as mentioned above have been developed in order to deal with these types of events. The currently favoured two methods are, the fully informed particle swarm [75] or the SVD (singular-value decomposition) matrix method [77, 78, 82, 83]. The former method is faster but the latter gives a better precision on the location of the hits. All these new algorithms still have to be validated with AGATA data. Given the absence of a one-for-all algorithm a dispatcher code, choosing the most adequate PSA algorithm for a given event, will also be implemented soon.

Table 10 gives an overview on the performance of different algorithms derived from tests using simulated data. The CPU performance is quoted relative to the grid-search algorithm (3 ms per event) for single interactions and the particle-swarm algorithm (2 ms to 5 ms per event) for multiple interactions.

After the energy calibration, which is done by the front-end electronics, the influence of noise, pedestal, time jitter and cross talk needs to be understood in order for the experimental signals to be successfully compared with the basis signals

Concerning the time jitter, different time-shift determination methods have been considered: supplementation of the basis with time-shifted signals, Neural Network determination [75], Kolmogorov-Smirnov determination [86], Taylor expansion and the substitution of residue minimisation by chi-square minimisation [87, 88]. The first method has the drawback of requiring larger signal bases, the latter method reduces the influence of the time jitter but does not measure it. Using simulated data, the Neural Network algorithm has shown to be very fast and provides a resolution better than 2 ns at computing times in the order of 10  $\mu\text{s}$ . Taking into account only the core signal, this algorithm seems to be very robust and hardly affected by noise and cross talk discussed below. The Kolmogorov-Smirnov and Taylor expansion methods are purely algebraic. They also give excellent results in terms of computing speed, robustness and precision.

The cross-talk effect is present in any segmented detector. It induces energy shifts and decreases the hit-location precision as it mixes the transient signals. Transient signals are those induced on adjacent electrodes to the primary interaction due to the drift of the charge carriers inside the germanium crystal. Cross-talk contributions can also appear between segments of different detectors. Only negligible cross-talk components were observed between a firing detector and the core signal of a neighbouring detector [22, 62]. The effects of cross talk are described in details in section 3. Two quite similar correction methods have been used. The first one



Table 4: Overview of the performance of different PSA algorithms derived from tests using simulated data. The performance is quoted relative to the grid-search algorithm. The position resolution is quoted in as FWHM values.

Algorithm	Single interaction		Multiple interactions	
	CPU time [norm/GS]	Resolution [mm]	CPU time [norm/PS]	Resolution [mm]
Grid search (GS) [57]	1	2	–	4 <sup>a</sup>
Extensive GS [75]	2.7	1	$6 \cdot 10^4$	4
Particle swarm (PS) [75]	0.1	2	1	4
Matrix method [77, 78]	6.7	2.4	10	10
Genetic algorithm [76]	330	1.9	$2 \times 10^2$	8.1
Binary search	0.06	1	Not adapted	Not adapted
Recursive subtraction [84, 85]	Not evaluated	3 <sup>b</sup>	Not evaluated	5 <sup>b</sup>
Neural network [75]	2	1.5	Not adapted	Not adapted
Wavelets	Not evaluated	2.3	Not adapted	Not adapted

<sup>a</sup> Only neighbouring segment hits.

<sup>b</sup> Only radial coordinate.

includes the cross-talk effect into the basis signal using a cross-talk matrix. The second corrects the measured signal by the cross-talk effect. These corrections permit the lowering of the FWHM error on the position by about 1 mm.

Another difficulty in the determination of the precise interaction position arises from the fact that the germanium crystal may be slightly displaced or tilted inside its capsule. It has been shown that this problem may be addressed prior to the experiment using the scanning tables or within the final setup using a radioactive source at fixed points and the  $\gamma$ -imaging method [89].

In order to facilitate the maintenance and development of algorithms used for AGATA two levels of abstraction are used for the PSA. The first is the ADF library [44] that is responsible for coding and decoding data in the data flow. The second layer of abstraction is a set of C++ classes, which provide, via inheritance, simple means of “attaching” a PSA algorithm to the Narval DAQ. This system has been successfully tested with the grid-search algorithm. Due to the fact that no cross correlations between the signals of different AGATA crystals has been found so far, all the PSA relevant algorithms operate on the signals of each individual crystal in parallel on different machines. This allows the use of several computers in parallel to analyse different events. Currently, it is foreseen to use 2 processors with 4 cores each to process the data of one crystal which will improve the PSA performance by a factor of 2 to 4.

Finally the events have to be reassembled according to their timestamps and a tracking algorithm is applied

in order to disentangle the coincident interaction points and to determine the total energy and the emission direction of those  $\gamma$  rays that have been fully absorbed in the germanium shell. Absolute positions of the individual crystals, tilting angles and target position corrections enter at this stage.

## 11. Gamma-ray tracking

The aim of tracking algorithms is to reconstruct the trajectories of the incident photons in order to determine their energy and direction. To do this, the algorithms must disentangle the interaction points identified in the detectors and establish the proper sequences of interaction points. Tracking algorithms can be divided into two classes: algorithms based on back tracking [90] and algorithms based on clustering and forward tracking [91]. Both are related to the particular properties of the interaction of photons with matter. In forward-tracking algorithms, the first step of the procedure is to group interaction points into clusters in  $(\theta, \phi)$  space. Back tracking, on the other hand, is based on the observation that the final photoelectric interaction after a  $\gamma$ -ray scattering sequence usually falls into a narrow energy band. Starting from interaction points in that energy range the algorithm tracks back towards the original emission point using the physical characteristics of the interaction process and selects the most probable interaction scheme.

For photon energies of interest (from about 10 keV to about 20 MeV), the main physical processes that occur when a photon interacts in germanium are Comp-

ton scattering, Rayleigh scattering, pair creation and the photoelectric interaction. Since Compton scattering is the dominant process between 150 keV and 10 MeV, all tracking algorithms are based on the properties of this interaction.

Within the AGATA project, the development and optimisation of tracking algorithms have been performed. Tracking has also been used to evaluate the performance of PSA. Another part of the work related to tracking has been the use of tracking techniques to investigate the background-suppression capabilities from sources of radiation that do not originate from the target.

### 11.1. Development of tracking algorithms

The development of tracking algorithms and the improvement of existing ones is an ongoing process. Realistic simulated data sets, produced with the GEANT4 AGATA code [14], have been and are systematically used to test, compare and improve the performance of tracking algorithms. This code treats the physics of the energy deposition correctly by generating and propagating all the possible secondary particles and by taking into account the momentum profile of electrons in germanium [92]. In order to produce more realistic data, the interaction points separated by less than  $d_{\text{res}} = 5$  mm are packed together, the positions of the interaction points are randomly shifted in all direction ( $x$ ,  $y$  and  $z$ ) by sampling a Gaussian energy-dependent uncertainty distribution and an energy threshold of 5 keV is applied to all the interaction points within each segment.

It has been shown that forward-tracking algorithms are more efficient than back-tracking ones [92]. This is because back-tracking algorithms rely on the identification of the last (photoelectric) interaction point in a scattering sequence, which generally loses its original characteristics after PSA: it is poorly localised and/or packed with other interaction points. However, ultimately the optimal  $\gamma$ -ray tracking algorithms may require the use of a combined approach where for example back tracking is used to recover events missed by the clustering techniques.

### 11.2. Clustering techniques

In the Mars Gamma-Ray Tracking (MGT) [93] and the Orsay Forward Tracking (OFT) [92] codes, both based on the forward-tracking technique, points are grouped into clusters according to their relative angular separation. In order to increase the tracking performance for high photon multiplicities without decreasing the performance at lower multiplicities, the maximum allowed separation angle is set to depend on the number of interaction points in the event.

A clustering technique based on the Fuzzy C-Means algorithm has been developed [94]. After running this algorithm, the optimal positions of the centres of the clusters and the degree of membership of each point to each of the clusters are obtained. The next step in the code is the “defuzzification”, making possible the use of standard validation procedures. Another clustering method, called Deterministic Annealing Filter (DAF), has also been developed [95]. In this method, the clustering problem is to perform the minimisation of the distortion criterion, which corresponds to the free energy related to the annealing process in statistical physics.

The detection efficiency and peak-to-total obtained by the above-mentioned algorithms for 1 MeV photons emitted at the centre of AGATA are summarised in Table 5.

Table 5: Simulated full-energy efficiency and peak-to-total (P/T) of AGATA for cascades of 30 (and 1) 1 MeV photons. In all the cases, the data is packed and smeared in the standard way and a 5 keV energy threshold has been applied.

Algorithm	Efficiency [%]	P/T [%]
MGT	28(43)	49(58)
OFT	24(37)	54(68)
Fuzzy C-Means	27	46
DAF	26(36)	47(69)

### 11.3. Effective distances

In all tracking philosophies, the photon trajectories are tracked with the help of the Compton scattering formula and with the ranges and cross sections of the photoelectric, Compton and pair-production interactions. To compute the appropriate ranges of photons in germanium, the effective distances in germanium between interaction points as well as between the interaction points and the source need to be computed. The problem can be solved analytically if the detector geometry is approximated to a  $4\pi$  germanium shell. This approximation was validated with the GEANT4 simulation code [14], in which the exact geometry of AGATA is defined, i.e. the shape of the crystals, encapsulation, cryostats, the empty spaces and the distances between all these elements.

### 11.4. PSA and front-end electronics

It has recently become clear that PSA algorithms have difficulties in dealing with events in which there

is more than one interaction point per segment. This is because the parameter space to search becomes very large and because the properties of the response function of the detector can lead to more than one solution. Although algorithms to determine the number of interaction points in each segment have been developed and have shown encouraging results in the coaxial part of the crystal [85], the effect of systematically assuming only one interaction point per segment has been implemented. No drastic drop in performance is observed, not even when the recoil velocity is 50 % of the speed of light, which yields a higher concentration of interaction points because of the Lorentz boost. This result is understood since the average of the distribution of the number of interaction points per segment is close to 1 and varies only slightly with incident photon energy.

Due to electronic noise, signals corresponding to a deposited energy below a certain value will not be detected in the segments of AGATA. The effect of this energy threshold on the tracking efficiency has been investigated. The loss in full-energy efficiency with respect to the case of a 1 keV threshold is found to be 1 % (5 keV threshold), 8 % (10 keV threshold), 13 % (20 keV threshold) and 29 % (50 keV threshold). The data from AGATA has shown that most of the full-energy efficiency can be recovered by using the core-energy information.

### 11.5. Neutrons

The influence of the elastic and inelastic interactions of neutrons on tracking performance has been found to be significant for low to medium  $\gamma$ -ray multiplicities especially on the P/T ratio [96]. As far as pulse shapes are concerned, it has been shown that neutrons and  $\gamma$  rays yield similar signals in nonsegmented closed-end coaxial and planar  $n$ -type HPGe crystals, even though the interaction mechanisms are different [97]. Distinguishing neutrons and  $\gamma$  rays by time of flight methods requires a timing resolution better than about 5 ns, which will be hard to achieve in the case of low-amplitude signals. Fingerprints of the neutron interaction points have been found, which may be used to reduce the background due to neutrons without too much loss in full-energy efficiency [98].

### 11.6. Scattering materials

The effect of passive materials in the inner space of the array, especially in connection with the used of complementary instrumentation, has been thoroughly discussed in Ref. [14]. The conclusion presented in this

work is that at medium or high  $\gamma$ -ray energies, the presence of scattering materials does not affect the performance of a tracking array more than in the case of a conventional array. However, at low energy Rayleigh scattering changes the direction of the incident photon, which directly affects the tracking process.

### 11.7. Imaging

The performance of PSA is generally tested by checking how well experimental spectra can be Doppler-corrected since this procedure directly depends on the attainable precision in locating each interaction point. Another method has recently been devised. It relies on Compton imaging, which does not need any beam nor complex experimental setup. Instead it is assumed that the quality of the image reconstruction obtained through the knowledge of the Compton scattering sequence in the detector can provide information on the interaction position resolution. The position and energy of the interaction points were extracted using the grid-search algorithm [57] assuming only 1 interaction point per segment. Since the incident energy is known, the first scattering angle can be extracted by selecting events according to their total energy and number of interaction points. This angle defines a scattering cone in 3D space. If more than one event is analysed, all the cones should overlap in a single point corresponding to the source of the  $\gamma$  rays. Placing the source far away from the detector reduces the problem to the forming of a 2D image on the surface of a sphere, which can be represented in a  $(\theta, \phi)$  plane. Comparison of the experimental and simulated  $\theta$  and  $\phi$  image profiles of a  $^{60}\text{Co}$  source has yielded an interaction position resolution of about  $\text{FWHM} = 5 \text{ mm}$  [99], which is comparable with the result obtained from in-beam experiments [79, 80, 100]. Attempts, using simple algorithms, to evaluate the capability of the AGATA detectors to reject  $\gamma$  rays originating from locations that are different from the target position have shown partial success [101].

### 11.8. Integration into the DAQ

Tracking is performed on 1 or 2 nodes of the PC farm of the AGATA DAQ, which runs the Narval system. The integration of the tracking and other algorithms into Narval were done by using the ADF library [44]. The goal is to make the data format transparent to the algorithms, i.e. ADF allows each algorithm to access the data it needs without knowing the structure of the data flow. It also provides a virtual Narval environment in which to test and debug algorithm codes in stand-alone mode. OFT and MGT are currently the only tracking

algorithms, which have been integrated into the Narval architecture. The online performance of OFT has been optimised and meets the specifications.

### 11.9. Tracked $^{60}\text{Co}$ spectrum

The results of a measurement with a  $^{60}\text{Co}$  source with three ATC detectors are shown in Fig. 40. The source was placed in the focal point of AGATA at a distance of 235 mm from the front face of the crystals. The black histogram shows a “raw” crystal spectrum obtained by summing all the individual gain-matched energy depositions in the crystal, corrected for segment threshold effects with the core-energy signal. The blue histogram is a tracked spectrum obtained by OFT and by excluding all single interaction points. The PSA was performed using the grid-search algorithm (see section 10) with the ADL pulse-shape database (see section 9). The P/T of the raw spectrum is 16.8 % using a low-energy cut-off of 0 keV. The P/T of the tracked spectrum is 53.9 % and 54.6 % using 0 keV and 200 keV cut-off values, respectively. The tracking efficiency, defined as the ratio of the number of counts in the full-energy peak in the tracked spectrum to the number of counts in the raw crystal spectrum, is 84.5 %.

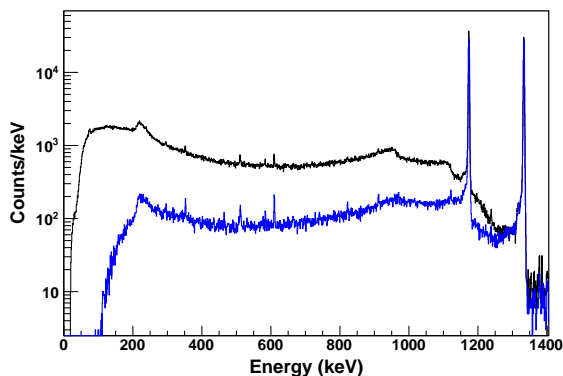


Figure 40: (Colour online)  $^{60}\text{Co}$  spectrum measured with three ATC detectors. Black histogram (greater number of counts): obtained by using the gain matched core signal of the crystals. Blue histogram (fewer number of counts): tracked spectrum excluding single interaction points. See text for further details.

## 12. Data analysis

As described in section 8, at the end of the AGATA DAQ chain, coincidences between tracked  $\gamma$  rays and ancillaries are provided. Data analysis needs to be performed at several stages, including replaying the full experiment from the raw traces. To help in these tasks a

package called GammaWare (GW) [47] has been developed.

The GW package is divided into several sub-projects: *Core*, *Physics*, *GEM* (Gamma-ray Event Monte Carlo), *Tools*, *ADF*, *ADFE* (Extended ADF library). A dynamic library, written in C++, is associated to each specific part. All libraries, except *ADF*, are based on the ROOT framework [102]. As a collaborative software, GW is available through the open-source version control system *subversion* and uses a bugtracker system. User’s documentation and web documentation, made by *doxygen*, can be found at the AGATA data-analysis web site [47].

The GW package adds facilities to ROOT that are specific to analysis of  $\gamma$ -ray spectroscopy data. Only the most significant add-ons are described here. The *Core* library contains facilities common to all sub-projects. The *Physics* library defines C++ objects specific to  $\gamma$ -ray spectroscopy analysis such as level schemes. As any ROOT object, a level scheme can be displayed and saved in ROOT files. They can be built graphically or imported from ENSDF [103] and RadWare [104] files. As an example, using the graphical level scheme display, gates are selected and then applied on correlated spaces, which are (virtual C++) interfaces to any kind of system storing  $\gamma$ -ray coincidences ( $\gamma^n$ ). So far  $\gamma$ - $\gamma$  ( $\gamma^2$ ) like matrices are implemented but the system is designed to be extendable to higher coincidence orders. From level schemes, cascades of discrete  $\gamma$  rays can be randomly generated and these cascades can be fed into GEANT4 simulations: the *GEM* sub-project is devoted to physics generators. In the *Tools* library many useful facilities can be found. It is the place where links to other data analysis frameworks are implemented, allowing for instance to ease exchanges of 1D and 2D spectra.

The GW package includes the *ADF* library (see section 8), which can be used also in stand-alone mode. Such a library contains a complete virtual interface to any actor processing the AGATA data flow. It defines the format of the data that are exchanged between the AGATA algorithms: they are encapsulated in frames with a trigger mechanism to deliver to a particular algorithm only the specified frames.

All the C++ actors processing the data flow are grouped in a package consisting of several dynamic libraries that are loaded into Narval. The actors can also be used in any other framework, in particular ROOT/GW, as well as linked to build a standard executable program. Some actors can process the data flow and moreover perform first stage analyses (counting rates, histograms, even traces saved in ROOT or ASCII files) to check online that the system is running

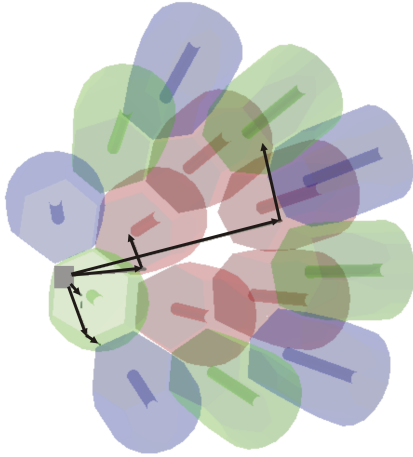


Figure 41: (Colour online) Online tracking Watcher display showing typical Compton scattering events in the 15 Ge crystals of AGATA, as provided by the tracking algorithm. Only the first and second interaction points are displayed.

properly.

In the GW package, the *ADF* library is extended through the *ADFE* sub-project bringing the AGATA like data to the ROOT/GW environment. In particular Watchers are defined there. They are light tasks dedicated to specific frames (output of an algorithm) running independently and easy to plug whatever the data flow structure is. A typical goal of the Watchers is to build histograms/graphs, to calibrate events from ancillary detectors. It is also used to save data in ROOT trees and to display events in 3D geometries via the ROOT/EVE facility. This is illustrated in Fig. 41 in which Compton events as provided on-line by the tracking algorithm can be visualised. The spy mechanism proposed by Narval (section 8) allows the same Watchers to be used on-line/offline and allows analysis to be performed at all stages of the data flow: signals (core and segments), hits distributions, raw data from the AGAVA card, counting rates, etc.

The virtualisation provided by the *ADF* library allows for the development of emulators, i.e. actors connected together within a common environment in various topologies as it is done in Narval [45]. Contrary to Narval, emulators only run so far on single computers and are not efficient in case of complex situations despite the fact that some of them run in multi-threading mode. However, as they are written in C/C++, it makes the development, testing, and debugging phases of the AGATA data-processing algorithms easier. Most of the actors are shared libraries that can be plugged in Narval

or in emulators. For efficiency reasons the event builder and the merger running online are written in Ada so they cannot be used as such for offline purposes. To overcome this problem, specific C++ actors have been developed to reproduce event builders and mergers as they act online. Emulators provide also elegant solutions to build almost any kind of complex analysis chain. Simple ones are used in the GW package to launch Watchers. More complete ones have been developed as for example the emulator of the whole topology as defined for the actual experiments.

### 12.1. Data processing on the Grid

The AGATA collaboration has adopted the Grid technologies [105] and has created its own virtual organisation (VO), namely `vo.agata.org`. The Grid computing resources (tape, disk and CPU) are presently provided by Lyon, Strasbourg, Paris and Valencia and are shared and accessed by the VO members under agreed common policies.

As mentioned in section 8, the raw data containing the preamplifier traces are recorded on a Grid tape-storage system at Tier1 sites for future off-line replay using, for instance, more sophisticated PSA and tracking algorithms than those implemented to run online. About 150 TB of data have been produced during the commissioning and the first experiments performed with up to 15 crystals during the period from March 2009 to September 2011, with an average value of 8 TB of data collected per experiment.

Besides the storage space question, partly discussed in [106], the transfer of the raw data to local institutes for analysis, as well as their processing, are also critical issues as they are very time and resource consuming. As the raw data have been stored on the Grid, then it is advisable to use also the Grid computing power (CPU) to replay the data, by emulating all or part of the DAQ system processing stages.

It has been demonstrated that replaying raw data on the Grid using an emulator is feasible without the need of changing the software to run on the Grid [107]. This is the case as long as copies of the input data files are previously downloaded into the node where the emulator is running, so the data are accessed locally. However, in the framework of designing a Grid computing model for data management and data processing for AGATA [108], more developments have been recently tested in order to access directly the data on the Grid storage [109]. For this, the emulator software has been modified by including the necessary functions from the Grid File Access Library (GFAL) in order to interact with the

Grid storage resource managers, through the appropriate protocols.

In the following, an example is presented in order to illustrate the performances in execution times for replaying raw data on the Grid. Three tasks of 49, 70 and 140 jobs, respectively, have been run on the IFIC/GRID-CSIC e-science infrastructure, each job executing an instance of the emulator that processes PSA and tracking on a fraction of the considered raw data set. It is worth noting that this infrastructure provides a distributed file system, namely Lustre, which allows direct access to the data located at the Grid storage of the site, without using GFAL. A total of respectively 2, 3 and 6 TB of commissioning data (147, 210 and 420 data files of 14 GB each, about  $10^8$  events) have been processed. Fig. 42 shows the evolution with time of the execution of the jobs for the above defined tasks. The average values of time measured for the completeness of the tasks, obtained from re-submitting them to Grid several times, are 3, 7 and 15 hours to process 2, 3 and 6 TB data, respectively. These results indicate that 8 TB of data, produced in a typical experiment, can be processed in less than one day.

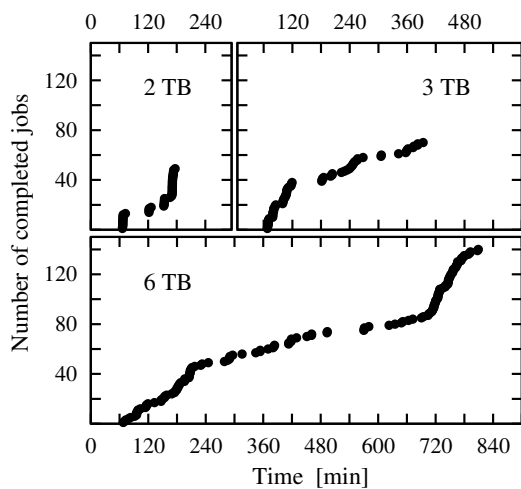


Figure 42: Completed jobs of data processing for 3 tasks run on the Grid as a function of time. Each job runs an instance of the emulator to replay part of the AGATA raw data set of interest.

### 13. Summary and outlook

The realisation of the AGATA spectrometer is a result of many technological advances. These range from advances in Ge detector technology, digital DAQ systems, signal decomposition and  $\gamma$ -ray interaction reconstruction, and in many areas of the infrastructure needed to support and operate such a complex device.

The AGATA spectrometer is now fully operational in its first physics campaign at INFN LNL in Legnaro, Italy, utilizing the wide range of stable beams available. A view of AGATA at the target position of the PRISMA spectrometer is shown in Fig. 43. AGATA is designed to be a peripatetic instrument and will move between major laboratories in Europe to take advantage of the range of different beams and equipment at each laboratory and of the resulting scientific opportunities. AGATA will be operated in a series of campaigns, the one first at LNL, and subsequently at the GSI facility in Germany and the GANIL laboratory in France. At GSI, AGATA will be used at the exit of the Fragment Separator (FRS) to study very exotic nuclei produced following high-energy fragmentation and secondary Coulomb excitation. At GANIL it will use the wide range of radioactive ions from the coupled cyclotrons and SPIRAL. During these first three physics campaigns the array will continually increase its efficiency as more detector systems are added. The first stage is to build up the system to 60 detector crystals, and then proceed towards the full implementation of the  $4\pi$  AGATA. Subsequent physics campaigns will take advantage of the new radioactive beams available as facilities such as FAIR, SPIRAL2, SPES and HIE-ISOLDE come online.

AGATA will have an enormous impact on nuclear physics research in particular the exploration of nuclear structure at the extremes of isospin, mass, angular momentum, excitation energy, and temperature. This radically new device will constitute a dramatic advance in  $\gamma$ -ray detection sensitivity that will enable the discovery of new phenomena in nuclei, which are only populated in a tiny fraction of the total reaction cross section or that are only produced with rates of the order of a few per second or less. The unprecedented angular resolution afforded by its position sensitivity will facilitate high-resolution spectroscopy with fast and ultra-fast fragmented beams giving access to the detailed structure of the most exotic nuclei that can be reached. In addition, the capability to operate at much higher event rates will allow the array to be operated for reactions with intense  $\gamma$ -ray backgrounds.

The instrumentation and technical advances driven by this work, and the knowledge gained by those involved, is also important in a wide range of applications. These advances have potential impact in areas such as medical imaging systems, homeland security, environmental monitoring and the nuclear industry.

In addition to the technical advances, AGATA represents a tremendous human achievement in the successful collaboration of several hundred personnel in 12 countries and over 40 laboratories and institutes across

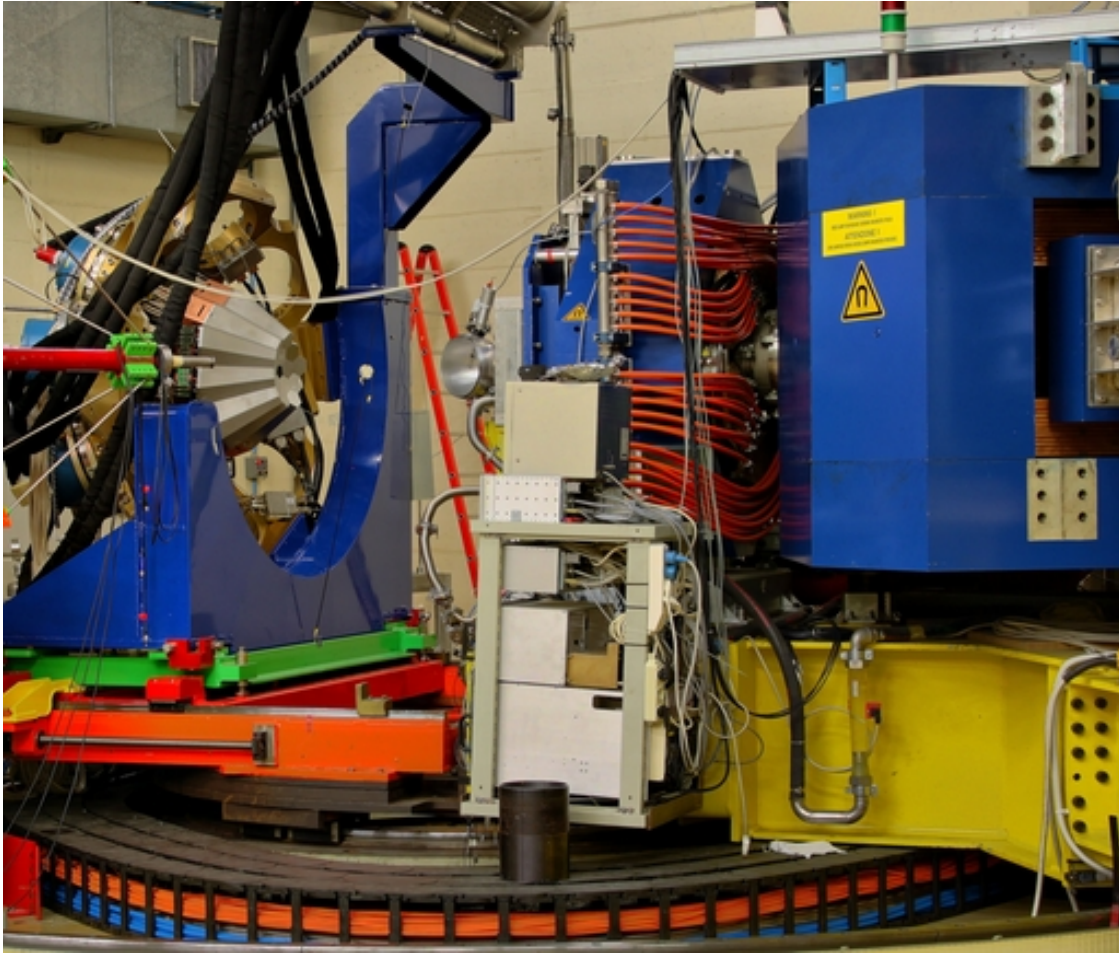


Figure 43: (Colour online) The AGATA and PRISMA spectrometers at LNL. The beam from the accelerators enters from the left. A part of the beam line, close to AGATA and half the scattering chamber has been removed. The quadrupole and dipole magnets of PRISMA are seen on the right-hand side of the photograph.

Europe. The collaboration is now excited with the prospect of using this spectrometer and to capitalise on its discovery potential for the understanding of the atomic nucleus.

#### 14. Acknowledgments

AGATA and this work is supported by the European funding bodies and the EU Contract RII3-CT-2004-506065, the German BMBF under Grants 06K-167 and 06KY205I, the Swedish Research Council and the Knut and Alice Wallenberg Foundation, UK EPSRC Engineering and Physical Sciences Research Council, UK STFC Science and Technology Facilities Council, AWE plc, Scientific and Technological Research Council of Turkey (Proj. nr. 106T055)

and Ankara University (BAP Proj. nr. 05B4240002), the Polish Ministry of Science and Higher Education under Grant DPN/N190/AGATA/2009, the Spanish MICINN under grants FPA2008-06419 and FPA2009-13377-C02-02, the Spanish Consolider-Ingenio 2010 Programme CPAN (contract number CSD2007-00042), and the Generalitat Valenciana under grant PROMETEO/2010/101. A. Gadea and E. Farnea acknowledge the support of MICINN, Spain, and INFN, Italy, through the AIC10-D-000568 bilateral action.

#### References

- [1] J. Sharpey-Schafer and J. Simpson, *Prog. Part. Nucl. Phys.* 21 (1988) 293 – 400.
- [2] C. Beausang and J. Simpson, *J. Phys. G* 22 (1996) 527–558.
- [3] F. Beck, *Prog. Part. Nucl. Phys.* 28 (1992) 443 – 461.

- [4] J. Simpson, *Z. Phys. A* 358 (1997) 139–143.
- [5] I. Lee, *Nucl. Phys. A* 520 (1990) C641–C655.
- [6] M. A. Deleplanque et al., *Nucl. Instr. Meth. A* 430 (1999) 292–310.
- [7] I. Y. Lee, M. A. Deleplanque, and K. Vetter, *Rep. Prog. Phys.* 66 (2003) 1095.
- [8] I. Lee et al., *Nucl. Phys. A* 746 (2004) 255C–259C.
- [9] J. Eberth et al., *Prog. Part. Nucl. Phys.* 46 (2001) 389–398.
- [10] D. Habs et al., *Prog. Part. Nucl. Phys.* 38 (1997) 111–126.
- [11] T. Kröll and D. Bazzacco, *Nucl. Instr. Meth. A* 463 (2001) 227–249.
- [12] R. Lieder et al., *Nucl. Phys. A* 682 (2001) 279–285.
- [13] R. Lieder et al., *Prog. Part. Nucl. Phys.* 46 (2001) 399–407.
- [14] E. Farnea et al., *Nucl. Instr. Meth. A* 621 (2010) 331–343.
- [15] J. Eberth et al., *Nucl. Instr. Meth. A* 369 (1996) 135–140.
- [16] S. Agostinelli et al., *Nucl. Instr. Meth. A* 506 (2003) 250–303.
- [17] A. Wiens et al., *Nucl. Instr. Meth. A* 618 (2010) 223–233.
- [18] D. Lersch et al., *Nucl. Instr. Meth. A* 640 (2011) 133–138.
- [19] A. Pullia, F. Zocca, and G. Pascovici, *IEEE Trans. Nucl. Sci.* (2006) 2869–2875.
- [20] F. Zocca et al., *IEEE Trans. Nucl. Sci.* (2009) 2384–2391.
- [21] G. Pascovici et al., *WSEAS Trans. Circ. Syst.* 7 (2008) 470–481.
- [22] B. Bruyneel et al., *Nucl. Instr. Meth. A* 599 (2009) 196–208.
- [23] B. Bruyneel et al., *Nucl. Instr. Meth. A* 608 (2009) 99–106.
- [24] J. Eberth and J. Simpson, *Prog. Part. Nucl. Phys.* 60 (2008) 283–337.
- [25] M. Descovich et al., *Nucl. Instr. Meth. A* 553 (2005) 535–542.
- [26] I. Lazarus et al., *IEEE Trans. Nucl. Sci.* 51 (2004) 1353–1357.
- [27] M. Dimmock et al., *IEEE Trans. Nucl. Sci.* 56 (2009) 1593–1599.
- [28] M. Dimmock et al., *IEEE Trans. Nucl. Sci.* 56 (2009) 2415–2425.
- [29] T. Ha et al., *Eur. Phys. J. A* (2011), submitted.
- [30] T. Ha, *Caractérisation des détecteurs d’AGATA et Etude de l’Hyperdéformation Nucléaire dans la Région de Masse 120*, Ph.D. thesis, Université Paris-Sud 11, Orsay, France (2009).
- [31] F. C. L. Crespi et al., *Nucl. Instr. Meth. A* 593 (2008) 440–447.
- [32] C. Domingo-Pardo et al., *Nucl. Instr. Meth. A* 643 (2011) 79–88.
- [33] N. Goel et al., *Nucl. Instr. Meth. A* 652 (2011) 591–594, *symposium on Radiation Measurements and Applications (SORMA) XII 2010*.
- [34] J. Tickner, M. Currie, and G. Roach, *Appl. Radiat. Isot.* 61 (2004) 67–71.
- [35] J. Gerl et al., *Nucl. Instr. Meth. A* 525 (2004) 328–331.
- [36] C. Domingo-Pardo et al., *IEEE Trans. Med. Imaging* 28 (2009) 2007–2014.
- [37] A. Stefanini et al., *Nucl. Phys. A* 701 (2002) 217–221.
- [38] A. Gadea et al., *Nucl. Instr. Meth. A* (2011), in print.
- [39] A. Georgiev and W. Gast, *IEEE Trans. Nucl. Sci.* 40 (1993) 770–779.
- [40] L. Arnold et al., *IEEE Trans. Nucl. Sci.* 53 (2006) 723–728.
- [41] PICMG 3.0 Revision 2.0 AdvancedTCA Base Specification, <http://www.picmg.org/>.
- [42] J. Simpson et al., *Acta Phys. Hung. New Ser.-Heavy Ion Phys.* 11 (2000) 159–188.
- [43] I. Lazarus et al., *IEEE Trans. Nucl. Sci.* 48 (2001) 567–569.
- [44] O. Stezowski, *AGATA Data Flow Library*, [http://agata.in2p3.fr/doc/ADF\\_DesignProposal.pdf](http://agata.in2p3.fr/doc/ADF_DesignProposal.pdf), unpublished.
- [45] X. Grave et al., *14th IEEE-NPSS Real Time Conf.* (2005) 119–123.
- [46] Narval web site, <http://narval.in2p3.fr/>.
- [47] O. Stezowski and the AGATA Data Analysis Team, *GammaWare User’s Guide*, <http://agata.in2p3.fr/doc/GwUserGuide.pdf>, unpublished.
- [48] ELOG web site, <http://midas.psi.ch/elog/>.
- [49] F. Lelli and G. Maron, *Distributed Cooperative Laboratories: Networking, Instrumentation and Measurements*, Springer-Verlag New York Inc., New York, USA (2006) 269–277.
- [50] J. Grebosz, *Comp. Phys. Commun.* 176 (2007) 251–265.
- [51] GRU/ViGRU documentation, <http://wiki.ganil.fr/gap/wiki/Documentation/Gru/Gru/>.
- [52] ENX web site, <http://enx.in2p3.fr/>.
- [53] Debian web site, <http://www.debian.org/>.
- [54] AGATA DAQ web site, <http://csngwinfo.in2p3.fr/>.
- [55] Zabbix web site, <http://www.zabbix.com/>.
- [56] Xen web site, <http://www.xen.org/>.
- [57] R. Venturelli and D. Bazzacco, *LNL Annual Report 2004*, INFN-LNL, Legnaro, Italy (2005) 220.
- [58] P. Médina, C. Santos, and D. Villaume, *Proc. 21st IEEE Instr. Meas. Tech. Conf.* 3 (2004) 1828–1832.
- [59] M. Schlarb et al., *Eur. Phys. J. A* (2011), submitted.
- [60] B. Bruyneel, P. Reiter, and G. Pascovici, *Nucl. Instr. Meth. A* 569 (2006) 764–773.
- [61] B. Bruyneel, P. Reiter, and G. Pascovici, *Nucl. Instr. Meth. A* 569 (2006) 774–789.
- [62] B. Bruyneel, *Characterization of Segmented Large Volume, High Purity Germanium Detectors*, Ph.D. thesis, Universität zu Köln, Cologne, Germany (2006), <http://kups.uni-koeln.de/1858/>.
- [63] B. Bruyneel, *Detector Simulation Software ADL*, <http://www.ikp.uni-koeln.de/research/agata/index.php?show=download>, unpublished.
- [64] V. Radeka, *Ann. Rev. Nucl. Part. Sci.* 38 (1988) 217–277.
- [65] L. Mihailescu et al., *Nucl. Instr. Meth. A* 447 (2000) 350–360.
- [66] Z. He, *Nucl. Instr. Meth. A* 463 (2001) 250–267.
- [67] B. Birkenbach et al., *Nucl. Instr. Meth. A* 640 (2011) 176–184.
- [68] B. Bruyneel, B. Birkenbach, and P. Reiter, *Nucl. Instr. Meth. A* 641 (2011) 92–100.
- [69] B. Bruyneel et al., *LNL Annual Report 2010*, INFN-LNL, Legnaro, Italy (2011) 64–65.
- [70] *Open CASCADE Technology, 3D modeling & numerical simulation*, <http://www.opencascade.org/>.
- [71] C. Geuzaine and J.-F. Remacle, *Int. J. Numer. Methods Eng.* 79 (2009) 1309–1331.
- [72] B. Kirk et al., *Engineering with Computers* 22 (2006) 237–254.
- [73] M. Galassi et al., *GNU Scientific Library Reference Manual – Third Edition (v1.12)*, Network Theory Limited, United Kingdom (2009).
- [74] J. Ljungvall, *Characterisation of the Neutron Wall and of Neutron Interactions in Germanium-Detector Systems*, Ph.D. thesis, Uppsala University, Uppsala, Sweden (2005), <http://urn.kb.se/resolve?urn=urn:nbn:se:uu:diva-5845>.
- [75] M. Schlarb, *Simulation and Real-Time Analysis of Pulse shapes from highly segmented Germanium detectors*, Ph.D. thesis, Technical University Munich, Munich, Germany (2008), <http://www.e12.physik.tu-muenchen.de/groups/agata/>.
- [76] T. Kröll and D. Bazzacco, *Nucl. Instr. Meth. A* 565 (2006) 691–703.
- [77] A. Olariu, *Pulse Shape Analysis for the Gamma-ray Tracking Detector AGATA*, Ph.D. thesis, Université Paris-Sud 11, Orsay France (2007).
- [78] A. Olariu et al., *IEEE Trans. Nucl. Sci.* 53 (2006) 1028–1031.
- [79] F. Recchia et al., *Nucl. Instr. Meth. A* 604 (2009) 555–562.
- [80] P.-A. Söderström et al., *Nucl. Instr. Meth. A* 638 (2011) 96–109.
- [81] S. Klupp, *A Calibration Experiment for the AGATA Pulse*



- Shape Analysis, Master's thesis, Technical University Munich, Munich, Germany (2011), <http://www.e12.physik.tu-muenchen.de/groups/agata/>.
- [82] P. Désesquelles et al., 14th IEEE-NPSS Real Time Conf. (2005) 100–102.
- [83] P. Désesquelles et al., *Eur. Phys. J. A* 40 (2009) 237–248.
- [84] F. C. L. Crespi, HPGe segmented detectors in  $\gamma$ -ray spectroscopy experiments with exotic beams, Ph.D. thesis, Università degli Studi di Milano (2008), <http://hdl.handle.net/2434/152528>.
- [85] F. Crespi et al., *Nucl. Instr. Meth. A* 570 (2007) 459 – 466.
- [86] P. Désesquelles et al., *Eur. Phys. J. A* 40 (2009) 249–253.
- [87] P. Désesquelles et al., *Nucl. Instr. Meth. B* 267 (2009) 542 – 547.
- [88] P. Désesquelles et al., *J. Phys. G* 36 (2009) 037001.
- [89] F. Recchia, In-beam test and imaging capabilities of the AGATA prototype detector, Ph.D. thesis, Università degli Studi di Padova, Padova, Italy (2008), <http://npgroup.pd.infn.it/Tesi/PhD-thesisRecchia.pdf>.
- [90] J. van der Marel and B. Cederwall, *Nucl. Instr. Meth. A* 437 (1999) 538 – 551.
- [91] G. J. Schmid et al., *Nucl. Instr. Meth. A* 430 (1999) 69 – 83.
- [92] A. Lopez-Martens et al., *Nucl. Instr. Meth. A* 533 (2004) 454 – 466.
- [93] D. Bazzacco, *Nucl. Phys. A* 746 (2004) 248 – 254, proceedings of the Sixth International Conference on Radioactive Nuclear Beams (RNB6).
- [94] G. Suliman and D. Bucurescu, *Rom. Rep. Phys.* 62 (2010) 27 – 36.
- [95] F. Didierjean, G. Duchêne, and A. Lopez-Martens, *Nucl. Instr. Meth. A* 615 (2010) 188 – 200.
- [96] J. Ljungvall and J. Nyberg, *Nucl. Instr. Meth. A* 550 (2005) 379 – 391.
- [97] J. Ljungvall and J. Nyberg, *Nucl. Instr. Meth. A* 546 (2005) 553 – 573.
- [98] A. Ataç et al., *Nucl. Instr. Meth. A* 607 (2009) 554 – 563.
- [99] F. Recchia et al., *Nucl. Instr. Meth. A* 604 (2009) 60 – 63.
- [100] P.-A. Söderström, Collective Structure of Neutron-Rich Rare-Earth Nuclei and Development of Instrumentation for Gamma-Ray Spectroscopy, Ph.D. thesis, Uppsala University, Uppsala, Sweden (2011), <http://urn.kb.se/resolve?urn=urn:nbn:se:uu:diva-149772>.
- [101] M. Doncel et al., *Nucl. Instr. Meth. A* 622 (2010) 614–618.
- [102] R. Brun and F. Rademakers, *Nucl. Instr. Meth. A* 389 (1997) 81 – 86.
- [103] J. Tuli, Evaluated Nuclear Structure Data File: A Manual for Preparation of Data Sets, BNL-NCS-51655-01/02-Rev (2001), <http://www.nndc.bnl.gov/nndcscr/documents/ensdf/#ensdf>.
- [104] D. C. Radford, *Nucl. Instr. Meth. A* 361 (1995) 297 – 305.
- [105] I. Foster and C. Kesselman, *The Grid: Blueprint for a New Computing Infrastructure*, Morgan Kaufmann Publishers, Inc., San Francisco, USA (1999).
- [106] V. Méndez et al., CLOSER 2011, Proceedings of the 1st International Conference on Cloud Computing and Services Science, Noordwijkerhout, The Netherlands, 507–511.
- [107] M. Kaci et al., IBERGRID 2010, Proceedings of the 4th Iberian Grid Infrastructure Conference, Braga, Portugal, 482–484.
- [108] M. Kaci and V. Méndez, The AGATA Grid Computing Model for Data Management and Data Processing, <http://ific.uv.es/grid/e-science/agata/gcm-dmdp.pdf>, unpublished.
- [109] M. Kaci et al., INGRID 2011, 6th Workshop for e-Science and e-Infrastructure, Santander, Spain.